Full length article

# Element mobilization and redistribution under extreme tropical weathering of basalts from the Hainan Island, South China

Ke Jiang[a,b], Hua-Wen Qi[a,*], Rui-Zhong Hu[a]

[a] *State Key Laboratory of Ore Deposit Geochemistry, Institute of Geochemistry, Chinese Academy of Sciences, Guiyang 550081, China*
[b] *University of Chinese Academy of Sciences, Beijing 100049, China*

A B S T R A C T

Chemical weathering of rocks has substantial influence on the global geochemical cycle. In this paper, the geochemical profile of a well-developed basalt weathering profile (> 15 m thick, including soil, saprolite, semi-weathered rock and fresh basalt) on the Island of Hainan (South China) was presented. The soil and saprolite samples from this profile are characterized by high $Al_2O_3$ and $Fe_2O_3$ concentrations (up to 32.3% and 28.5%, respectively). The mineral assemblage is dominated by kaolinite, Fe-oxides/-hydroxides and gibbsite (or boehmite), indicating extensive desilicate and ferrallitic weathering. The acidic and organic-rich environment in the soil horizon may have promoted elemental remobilization and leaching.

The strongest $SiO_2$ depletion and $Al_2O_3$ enrichment at about 2.4 m deep indicate that the main kaolinite hydrolysis and gibbsite formation occurred near the soil-saprolite interface. The mild Sr reconcentration at about 3.9 m and 7.1 m deep may be attributed to secondary carbonate precipitation. Mn-oxides/-hydroxides precipitated at 6.1 m deep, accompanied by the strongest enrichment of Ba and Co. Uranium is mildly enriched in the middle part (about 7.1 m and 9.1 m deep) of the weathering profile, and the enrichment may have been caused by the decomposition of uranyl carbonates or the accumulation of zircon. Immobile element (i.e., Zr, Hf, Nb, Ta, Th and Ti) distributions at different depths are mainly controlled by secondary Fe-oxides/-hydroxides, and follow the stability sequence of Nb ≈ Ta ≈ Th > Zr ≈ Hf > Ti. The limited thickness (~15 cm) of the semi-weathered basalt horizon at the rock-regolith interface (15.28 m deep) suggests that plagioclase and pyroxene are readily altered to kaolinite, smectite and Fe-oxides under tropical climate. The marked enrichment of transitional metals (such as Cu, Zn, Ni, and Sc) along the rock-regolith interface may have associated mainly with increasing pH values, as well as the dissolution of primary apatite and formation of secondary phosphates. Our findings highlight the importance of secondary phosphates in the redistribution of transition metals, and in the possible Mg, Cu, and Ni isotopic fractionation under extreme weathering of basalt in tropic climate.

## 1. Introduction

Chemical weathering of rocks is an important surficial geochemical process, and has contributed immensely to the modification of landmass morphology, chemical cycling of the oceans, atmospheric $CO_2$ consumption, and thus global carbon cycle and climate change (Nesbitt and Young, 1982; Berner et al., 1983; Berner and Berner, 1997; Kump et al., 2000; Dessert et al., 2003; Lerman et al., 2007; Scott et al., 2008; Gislason et al., 2009; Jha et al., 2009; Wang et al., 2016). Catchment and soil profile studies have been conducted to address the questions related to silicate weathering (Nesbitt and Young, 1989; Walter et al., 1995; Nesbitt and Markovics, 1997; Gaillardet et al., 1999; Viers et al., 2000; Pokrovsky and Schott, 2002; Pokrovsky et al., 2006; Ma et al., 2007; Navarre-Sitchler and Brantley, 2007; Jha et al., 2009; Babechuk

et al., 2014, 2015; Prunier et al., 2015; Liu et al., 2016). In particular, elemental behaviors (mobilization and reconcentration) and isotopic (e.g., Si, Li, Fe, Cu, Mg and Ni) fractionation during weathering are pivotal to understand the weathering mechanism and has thus attracted increasing attention in recent research (e.g., Ji et al., 2004; Pokrovsky et al., 2006; Georg et al., 2007; Ma et al., 2007; Teng et al., 2010; Feng, 2010; Huang et al., 2012; Babechuk et al., 2014, 2015; Liu et al., 2014; Wang et al., 2015).

Field and experimental research on the weathering profiles developed on different rock types demonstrates that during chemical weathering: (1) Alkali metals such as K, Na, Ca and Mg are highly mobile and are severely leached at the early weathering stage (Nesbitt et al., 1980; Babechuk et al., 2014); (2) Elements such as Zr, Hf, Nb, Ta, Ti and Th are immobile because of their resistate host minerals (e.g.,

zircon, rutile and anatase) (Kurtz et al., 2000; Balan et al., 2001; Hodson, 2002; Babechuk et al., 2015); (3) Elemental behaviors of redox sensitive elements (i.e. Mn, Co, Cr, Ce and U) are largely redox dependent (Guthrie and Kleeman, 1986; Middelburg et al., 1988; Collins and Kinsela, 2010; Kraemer et al., 2015; Zhang et al., 2015); and (4) Transition metals, such as Cu, Zn, and Ni, can be strongly adsorbed on secondary Fe/Mn-(hydro)oxides, and thus their concentrations are significantly influenced by the presence of the latter (Marques et al., 2004; Ling et al., 2015).

Basalts are readily weathered in tropical climate, with their primary minerals decomposed and chemical elements released (Nesbitt and Young, 1982; Gislason and Arnorsson, 1993). Therefore, basalt weathering profiles or residues represent good research target for elemental behaviors during chemical weathering and paleosol formation (Chesworth et al., 1981; Hill et al., 2000; Kurtz et al., 2000; Rye and Holland, 2000; Driese, 2004; Sak et al., 2004, 2010; Ma et al., 2007; Babechuk et al., 2014, 2015; Driese et al., 2016). For instance, the basalt weathering profiles developed in the northern Hainan Island have been studied previously on its primary/secondary mineral compositions (He et al., 2008; Jiang et al., 2011), the trace element (including REE) migration and redistribution (Huang and Gong, 2001; Ma et al., 2007), and the Sr-Nd-Hf, Fe, Mg and Cu isotope systematics (Ma et al., 2010; Huang et al., 2012; Liu et al., 2014). Most of the published works were conducted on the same basalt weathering profile (19°34.74′N, 110°38.71′E) firstly reported by Ma et al. (2007), which is not well-developed (only ~4.5 m deep) and incomplete (rock-regolith interface missing).

In this contribution, we conducted systematic field mapping and sampling across a well-developed and complete profile (including the soil, saprolite, semi-weathered basalt and fresh basalt horizons), and investigated the mineral and geochemical (major and trace element) stratigraphic variations across different depths of the weathering profile. With these new data, we establish the geological and geochemical weathering model, and discuss how major and trace elements are re-mobilized and redistributed under extreme weathering of basalt in tropical climate. Our results highlight the importance of secondary phosphates on the redistribution of transition metals (such as Cu, Zn, Ni, and Sc) and many other trace elements (i.e., Be and Cr).

## 2. Geological setting and sampling

The Island of Hainan is the biggest tropical island in South China. The tropical climate on the island is controlled by the East Asian monsoon, with average annual temperature of 25 °C (summer maximum temperature: 30–32 °C; winter minimum temperature: 18–20 °C) and annual rainfall of 800–2500 mm (average: 1500 mm), of which above 80% (rainfall) occurs during May to October (Ma et al., 2007). Cenozoic basalts are widely distributed in northern Hainan (Liu et al., 2015, Fig. 1a). Major rock types include tholeiitic basalt, basaltic andesite, alkaline basalt and dolerite. These basalts are commonly covered by laterite derived from basalt weathering.

The weathering profile studied is located in a quarry and developed on the Miocene-Pliocene tholeiitic basalt in southwestern Wenchang (19°34′47.0″N, 110°38′42.6″E, Fig. 1a and b). The profile (up to 19.73 m thick) can be divided into three horizons down depth (soil, saprolite and basalt). The rock-regolith interface is distinct and manifested by the presence of a horizon consists of 15 cm thick yellowish semi-weathered basalt, which overlies parallelly on the fresh basalt (no obvious gravel interbeds are found). The weathering profile is covered by vegetation. The top 2.4 m of the profile is made up of reddish homogenous soil. The color of the saprolite changes from deep red at 2.4--13.2 m to yellowish at 13.2–15.28 m (Fig. 1c).

The soil and saprolite sampling was conducted in a 15–20 cm spacing, and 12 soil samples (WC-1 to WC-12) and 40 saprolite samples (WC-13 to WC-52) were collected across different depths. One semi-weathered basalt (WC-53) and five fresh basalt (WC-54 to WC-58) were

sampled in a 0.6–1.3 m spacing. Samples near the top of the soil horizon contain plant roots and stems. The detailed profile and sample descriptions (including horizon, soil color, soil structure, influence of biological activity and soil particle size analysis results) were given in Table A1. The soil and saprolite samples collected were dried naturally, and milled to 200 mesh (< 75 μm) with a tungsten-carbide mill after removing the plant roots and stems.

## 3. Methods

### 3.1. XRD and SEM-EDS analyses

X-ray diffractometer (XRD) and scanning electron microscope with energy dispersive spectrometer (SEM-EDS) analyses on all the samples were performed at the State Key Laboratory of Ore Deposit Geochemistry, Institute of Geochemistry, Chinese Academy of Sciences (IGCAS). XRD was conducted by using a Rigaku D/Max 2200 Powder X-ray Diffractometer, with analytical conditions include CuKα radiation; graphite as filter, 40 kV accelerating voltage, and 30 mA current. XRD analytical results were given in Table 1. Small amount of representative soil and saprolite powder samples were analyzed by using a JEM-2000FX II SEM with build-in EDS, and the analysis conditions include up to 1 μm beam diameter, 30 kV accelerating voltage and ~10 mm working distance.

### 3.2. Major and trace element analyses

Major element analyses of all samples were conducted by using X-ray Fluorescence (XRF) at the ALS Laboratory in Guangzhou, China. Lithium-nitrate was added and mixed with the sample, and the mixed powder was then melted, poured into platinum crucibles and fused into glass beads. XRF analysis was conducted with a PANalytical Magix Fast machine, with detection limit of > 0.01%. The LOI (loss on ignition) values were determined by the weight loss after heating the samples to 1000 °C. Trace element analyses ware performed by using PE Elan DRC-e solution ICP-MS at the State Key Laboratory of Ore Deposit Geochemistry (IGCAS). About 50 mg of sample powder was weighted and placed into Teflon cups, and the sample was then decomposed by 1 ml HF and 0.5 ml $HNO_3$ at 185 °C for 24 h. After cooling and drying (and then re-drying after adding 1 ml $HNO_3$) over a hot plate, the residue was re-dissolved by 2 ml $HNO_3$ and 3 ml deionized water (500 ppb Rh were added) at 140 °C for 5 h. After cooling, 0.4 ml of the sample solution was transferred into a 15 ml centrifugal tube and diluted to 8–10 ml for the ICP-MS measurement. The standards used include the Chinese soil standards GSS-4 and GSS-7, together with the rock standards GSR-1 and AGV-2. Accuracies for the major and trace element analyses were better than 1% and 10%, respectively. Full analytical results were given in Table 2.

### 3.3. Carbon analyses and soil pH measurement

Total organic carbon (TOC), total carbon (TC) and inorganic carbon (IC) analyses were conducted at the State Key Laboratory of Environmental Geochemistry (IGCAS) with an Elementar Vario MACRO cube elemental micro-analyzer (Table 2). 1–2 g of the sieved (100 mesh) soil and saprolite samples were placed into a 50 ml centrifugal tube, and then soaked in 20 ml 1 mol/L HCl for 24 h to remove the inorganic carbon (shake every 8 h to maximize the reaction). The sample was then washed with $CO_2$-free deionized water to be neutral, and then dried in a freeze drier for 24 h. After that, 10–30 mg of the sample was weighted and placed into a tin cup for combustion. Impurities were removed and the remaining $N_2$, $CO_2$, $H_2O$ and $SO_2$ gases were transported (by He carrier gas) first into a gas mixing chamber and then into a thermal conductivity detector (of gas chromatography) for quantitative analysis. This carbon concentration was defined as TOC, while the carbon content obtained following the same procedure but
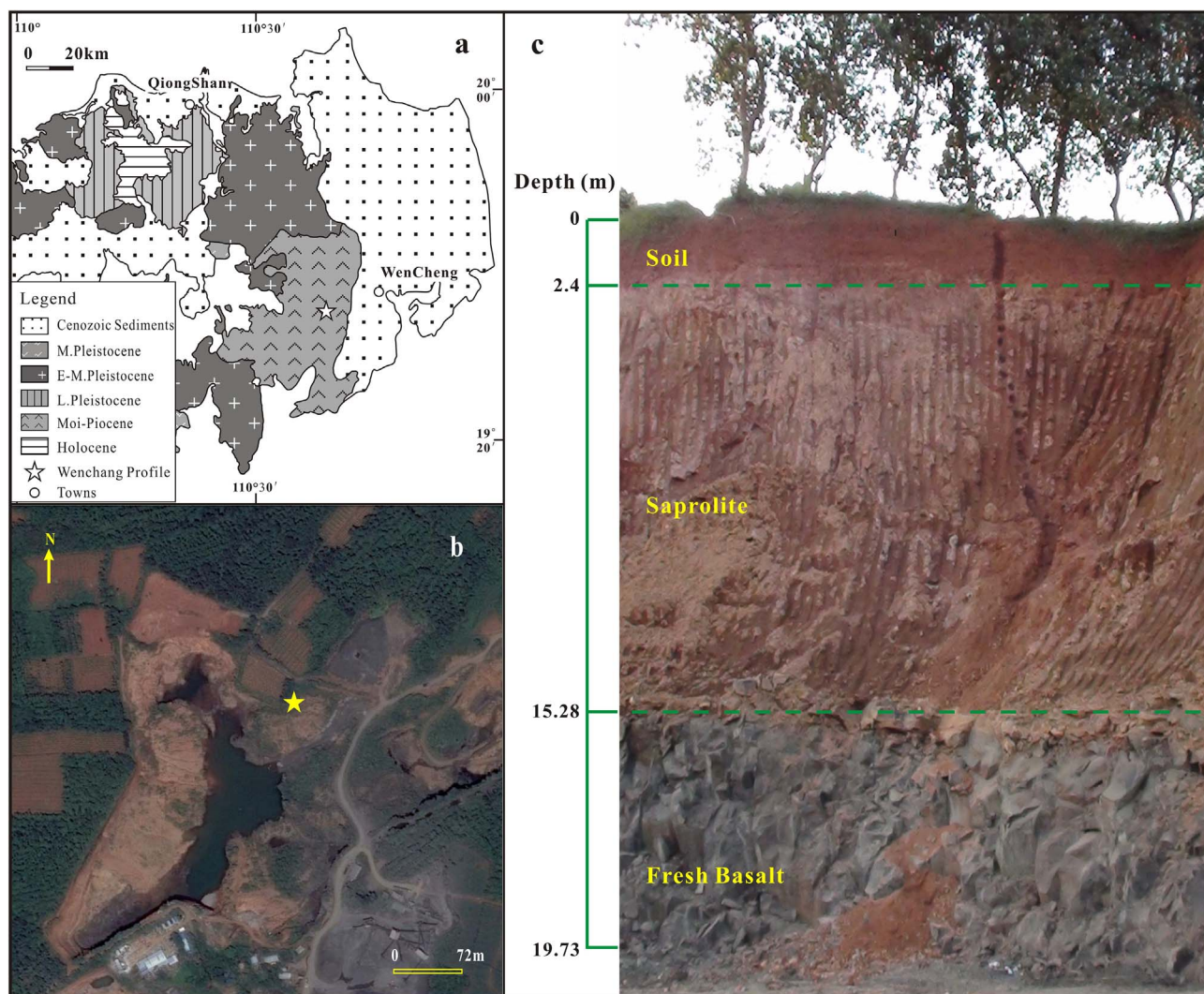
**Fig. 1.** (a) Simplified geologic map and sampling location in Wenchang, northern Hainan Island (modified after Liu et al., 2015); (b) Google Earth satellite image of the sampling site; (c) Outcrop photo of the Wenchang basalt weathering profile.

without HCl and $CO_2$-free deionized water treatment was defined as TC, and the difference between TC and TOC concentrations was treated as the concentration of inorganic carbon (IC). The accuracy for carbon analysis ranges from about 1% or ± 0.002% (1s) (for the samples with carbon content > 0.1%) to about 10% or ± 0.007% (1s) (for the samples with carbon content < 0.1%).

For the soil pH measurement, 10 g of the sieved (10 mesh) soil sample was placed into a 50 ml centrifugal tube, and 25 ml $CO_2$-free deionized water was added in a ratio of 1:2.5. The soil and water was well-mixed with a glass rod, settled for 30 min and then tested with a Sartorius PP-50 pH meter. Each sample was measured three times, and the average value was taken as the final result (Table 2). Measurement accuracy is better than 0.05.

### 3.4. Mass balance calculation

Mass balance calculation is widely used in assessing the elemental mobilization and redistribution during chemical weathering profile formation processes (Nesbitt, 1979; Nesbitt et al., 1980; Kurtz et al., 2000; Brantley and Lebedeva, 2011; Babechuk et al., 2014, 2015). The net gain and loss of a particular element (j) relative to the fresh parent rocks can be expressed as:

$$\tau_{i,j} = \frac{C_{j,w}}{C_{j,p}} \times \frac{C_{i,p}}{C_{i,w}} - 1$$

where $C_{j,w}$ and $C_{j,p}$ are the concentrations of element j in the weathered soil and fresh parent rock, respectively, and $C_{i,w}$ and $C_{i,p}$ are the concentrations of the relatively most stable element (i) in the weathered soil and fresh parent rock, respectively. A element-mass-transfer coefficient $\tau_{i,j} < 0$ would reflect a net loss of element j relative to the parent rock, and vice versa for $\tau_{i,j} > 0$. $\tau_{i,j} = 0$ would indicate that element j is stable and immobile.

The choice of the immobile element i depends on the rock types and climate. For instance, Nesbitt (1979) suggest that Ti is the most stable element in the weathering profiles of granites. Kurtz et al. (2000) consider that Nb and Ta are the most stable in the weathering profiles of basalts, whilst Ma et al. (2007) suggest that Th is the most stable element during extreme weathering of basalt. However, Babechuk et al. (2015) consider Th is unsuitable to be a reference element because of the possible aeolian input (Kurtz et al., 2000). Niobium was chosen as the most stable element i in the mass balance calculation of this study (see Section 5.4.2 and Appendix B). The average basalt composition and Nb concentration were adopted for the $C_{j,p}$ and $C_{i,p}$ of the fresh basaltic parent rocks, respectively.

**Table 1**
XRD mineral compositions of the samples from the Wenchang basalt weathering profile.

| Sample no. | Sample type | Depth (m) | Main mineral compositions |
|---|---|---|---|
| WC-1 | Soil | 0.1 | Kaolinite + Fe (hydro)oxides + Gibbsite |
| WC-2 | Soil | 0.3 | Kaolinite + Fe (hydro)oxides + Smectite + Gibbsite + Quartz |
| WC-3 | Soil | 0.5 | Kaolinite + Fe (hydro)oxides + Boehmite |
| WC-4 | Soil | 0.7 | Kaolinite + Smectite + Fe (hydro)oxides + Smectite |
| WC-5 | Soil | 0.9 | Kaolinite + Fe (hydro)oxides + Gibbsite |
| WC-6 | Soil | 1.1 | Kaolinite + Smectite + Fe (hydro)oxides + Gibbsite |
| WC-7 | Soil | 1.3 | Kaolinite + Smectite + Fe (hydro)oxides + Boehmite + Gibbsite |
| WC-8 | Soil | 1.5 | Kaolinite + Fe (hydro)oxides + Smectite |
| WC-9 | Soil | 1.7 | Kaolinite + Fe (hydro)oxides |
| WC-10 | Soil | 1.9 | Kaolinite + Fe (hydro)oxides + Gypsum + Gibbsite + Quartz |
| WC-11 | Soil | 2.1 | Kaolinite + Fe (hydro)oxides + Gibbsite |
| WC-12 | Soil | 2.4 | Gibbsite + Kaolinite + Fe (hydro)oxides |
| WC-13 | Saprolite | 2.8 | Kaolinite + Fe (hydro)oxides + Gibbsite |
| WC-14 | Saprolite | 3.1 | Kaolinite + Fe (hydro)oxides + Smectite |
| WC-15 | Saprolite | 3.5 | Kaolinite + Fe (hydro)oxides + Smectite |
| WC-16 | Saprolite | 3.9 | Kaolinite + Fe (hydro)oxides + Smectite + Illite |
| WC-17 | Saprolite | 4.4 | Kaolinite + Fe (hydro)oxides + Quartz |
| WC-18 | Saprolite | 4.9 | Kaolinite + Fe (hydro)oxides + Smectite + Illite |
| WC-19 | Saprolite | 5.3 | Kaolinite + Fe (hydro)oxides + Smectite + Quartz |
| WC-20 | Saprolite | 5.7 | Kaolinite + Fe (hydro)oxides + Quartz |
| WC-21 | Saprolite | 6.1 | Kaolinite + Fe (hydro)oxides + Quartz |
| WC-22 | Saprolite | 6.7 | Kaolinite + Fe (hydro)oxides + Smectite + Gypsum |
| WC-23 | Saprolite | 7.1 | Kaolinite + Fe (hydro)oxides + Quartz |
| WC-24 | Saprolite | 7.3 | Kaolinite + Fe (hydro)oxides + Smectite + Quartz |
| WC-25 | Saprolite | 7.5 | Kaolinite + Fe (hydro)oxides + Smectite + Illite + Quartz |
| WC-26 | Saprolite | 8 | Kaolinite + Fe (hydro)oxides + Smectite + Illite + Quartz |
| WC-27 | Saprolite | 8.4 | Kaolinite + Fe (hydro)oxides + Smectite + Illite + Quartz |
| WC-28 | Saprolite | 8.6 | Kaolinite + Fe (hydro)oxides + Smectite + Illite + Quartz |
| WC-29 | Saprolite | 8.8 | Kaolinite + Fe (hydro)oxides + Smectite + Illite + Boehmite |
| WC-30 | Saprolite | 9.1 | Kaolinite + Fe (hydro)oxides + Gypsum |
| WC-31 | Saprolite | 9.28 | Kaolinite + Fe (hydro)oxides + Smectite + Illite + Quartz |
| WC-32 | Saprolite | 9.56 | Kaolinite + Fe (hydro)oxides + Smectite |
| WC-33 | Saprolite | 9.84 | Kaolinite + Fe (hydro)oxides + Smectite + Illite + Quartz |
| WC-34 | Saprolite | 10.12 | Kaolinite + Fe (hydro)oxides + Smectite + Illite + Quartz + Boehmite |
| WC-35 | Saprolite | 10.4 | Kaolinite + Fe (hydro)oxides + Smectite + Illite + Quartz + Boehmite |
| WC-36 | Saprolite | 10.68 | Kaolinite + Fe (hydro)oxides + Quartz |
| WC-37 | Saprolite | 10.96 | Kaolinite + Fe (hydro)oxides + Smectite + Illite + Quartz |
| WC-38 | Saprolite | 11.24 | Kaolinite + Fe (hydro)oxides + Gypsum + Smectite + Illite + Quartz |
| WC-39 | Saprolite | 11.52 | Kaolinite + Fe (hydro)oxides + Smectite + Illite + Quartz |
| WC-40 | Saprolite | 11.8 | Kaolinite + Fe (hydro)oxides + Smectite + Illite + Quartz |
| WC-41 | Saprolite | 12.08 | Kaolinite + Fe (hydro)oxides + Smectite + Illite |
| WC-42 | Saprolite | 12.36 | Kaolinite + Fe (hydro)oxides + Smectite + Illite + Quartz |
| WC-43 | Saprolite | 12.64 | Kaolinite + Fe (hydro)oxides + Illite + Boehmite |
| WC-44 | Saprolite | 12.92 | Kaolinite + Fe (hydro)oxides + Smectite + Illite + Quartz |
| WC-45 | Saprolite | 13.2 | Kaolinite + Fe (hydro)oxides + Smectite + Illite + Quartz |
| WC-46 | Saprolite | 13.48 | Kaolinite + Fe (hydro)oxides + Smectite + Quartz |
| WC-47 | Saprolite | 13.76 | Kaolinite + Fe (hydro)oxides + Smectite + Illite + Quartz |
| WC-48 | Saprolite | 14.04 | Kaolinite + Fe (hydro)oxides + Smectite + Quartz |
| WC-49 | Saprolite | 14.32 | Kaolinite + Fe (hydro)oxides + Smectite + Chlorite + Illite + Quartz |
| WC-50 | Saprolite | 14.6 | Kaolinite + Fe (hydro)oxides + Smectite + Chlorite + Illite + Quartz |
| WC-51 | Saprolite | 14.88 | Kaolinite + Fe (hydro)oxides + Smectite + Chlorite + Illite + Quartz |
| WC-52 | Saprolite | 15.16 | Kaolinite + Fe (hydro)oxides + Smectite + Chlorite + Illite + Quartz |
| WC-53 | SWB[a] | 15.28 | Plagioclase + Pyroxene + Smectite + Chlorite + Quartz |
| WC-54 | Basalt | 15.83 | Plagioclase + Pyroxene + Smectite + Quartz |
| WC-55 | Basalt | 16.43 | Plagioclase + Pyroxene + Smectite + Quartz |
| WC-56 | Basalt | 17.43 | Plagioclase + Pyroxene + Smectite + Quartz |
| WC-57 | Basalt | 18.73 | Plagioclase + Pyroxene + Smectite + Quartz |
| WC-58 | Basalt | 19.73 | Plagioclase + Pyroxene + Smectite + Quartz |

[a] SWB = Semi-weathered basalt. Fe-oxides/hydroxides = goethite + hematite.

## 4. Results

### 4.1. Mineral compositions

The XRD diffraction spectra of the fresh basalt are very similar, and reveal the presence of mainly plagioclase (with a major narrow peak at 3.22 Å), pyroxene (confirmed by the peaks at 3.01, 2.95 and 2.53 Å) and minor quartz (with a peak at 3.37 Å) (Table 1; Fig. 2). The basalt also contains minor low-temperature alteration minerals such as smectite (weak peak at 15.0 Å). Semi-weathered basalt contains mainly amorphous minerals (confirmed by enhanced background of the XRD spectrum), including plagioclase, pyroxene and minor clay minerals, such as smectite and chlorite. Soil samples are mainly composed of amorphous minerals, including kaolinite (or halloysite) (confirmed by the peaks at 7.27, 4.43, 3.58 and 2.34 Å), gibbsite (with a major narrow peak at 4.82 Å), boehmite (with a peak at 6.1 Å), illite (with a peak near 10.0 Å), smectite and minor quartz, as well as Fe-oxides/hydroxides (e.g., goethite, hematite and limonite as suggested by the 4.18 Å, 2.71 Å, 2.52 Å and 2.44 Å peaks). Notably, kaolinite and halloysite dominate most saprolite samples, whereas gibbsite dominates the soil and saprolite samples around the soil-saprolite interface. In addition, some samples from the upper and middle parts of the weathering profile

**Table 2**

Major and trace element compositions, pH values and ratios of samples from Wenchang.

| Sample No. | WC-1 | WC-2 | WC-3 | WC-4 | WC-5 | WC-6 | WC-7 | WC-8 | WC-9 | WC-10 | WC-11 | WC-12 | WC-13 | WC-14 | WC-15 |
|---|---|---|---|---|---|---|---|---|---|---|---|---|---|---|---|
| Sample type | Soil | Soil | Soil | Soil | Soil | Soil | Soil | Soil | Soil | Soil | Soil | Soil | SP[c] | SP | SP |
| Depth (m) | 0.1 | 0.3 | 0.5 | 0.7 | 0.9 | 1.1 | 1.3 | 1.5 | 1.7 | 1.9 | 2.1 | 2.4 | 2.8 | 3.1 | 3.5 |
| $SiO_2$ (%) | 29.5 | 29.9 | 30.5 | 30.3 | 30.6 | 30.9 | 27.7 | 32.1 | 32.3 | 32 | 30.9 | 13.3 | 32.4 | 32.3 | 34.2 |
| $TiO_2$ (%) | 4.14 | 4.25 | 3.97 | 4.00 | 3.91 | 3.68 | 3.27 | 3.44 | 3.49 | 3.48 | 3.73 | 5.03 | 3.32 | 3.70 | 3.41 |
| $Al_2O_3$ (%) | 26.1 | 26.5 | 27.0 | 26.9 | 27.3 | 27.8 | 28.6 | 28.0 | 27.9 | 27.7 | 27.5 | 32.3 | 28.3 | 27.0 | 27.9 |
| $Fe_2O_3$ (%) | 22.2 | 22.9 | 22.5 | 22.5 | 22.6 | 22.4 | 24.2 | 21.6 | 21.7 | 21.6 | 22.7 | 28.5 | 20.9 | 22.3 | 19.6 |
| MnO (%) | 0.14 | 0.18 | 0.19 | 0.18 | 0.20 | 0.21 | 0.19 | 0.16 | 0.14 | 0.16 | 0.19 | 0.13 | 0.38 | 0.21 | 0.43 |
| $P_2O_5$ (%) | 0.42 | 0.25 | 0.22 | 0.22 | 0.22 | 0.22 | 0.25 | 0.21 | 0.22 | 0.22 | 0.36 | 0.64 | 0.34 | 0.25 | 0.20 |
| MgO (%) | 0.39 | 0.32 | 0.31 | 0.28 | 0.29 | 0.29 | 0.27 | 0.32 | 0.34 | 0.34 | 0.35 | 0.23 | 0.31 | 0.30 | 0.51 |
| CaO (%) | 0.18 | 0.02 | 0.01 | 0.02 | 0.02 | 0.02 | 0.01 | 0.01 | 0.02 | 0.02 | 0.01 | 0.02 | 0.01 | 0.01 | 0.01 |
| $Na_2O$ (%) | 0.07 | 0.01 | 0.01 | 0.01 | 0.01 | 0.01 | 0.02 | 0.01 | 0.01 | 0.01 | 0.01 | 0.02 | 0.01 | 0.01 | 0.01 |
| $K_2O$ (%) | 0.04 | 0.03 | 0.02 | 0.02 | 0.02 | 0.02 | 0.02 | 0.01 | 0.01 | 0.01 | 0.01 | < 0.01 | 0.01 | 0.01 | 0.01 |
| LOI (%) | 15.5 | 15.2 | 14.6 | 14.4 | 14.2 | 14.1 | 14.8 | 13.6 | 13.4 | 13.4 | 13.7 | 19.2 | 13.7 | 13.0 | 13.0 |
| Total (%) | 98.68 | 99.56 | 99.33 | 98.83 | 99.37 | 99.65 | 99.33 | 99.46 | 99.53 | 98.94 | 99.47 | 99.31 | 99.68 | 99.09 | 99.28 |
| Li (ppm) | 3.56 | 3.69 | 3.98 | 3.96 | 3.65 | 3.85 | 3.82 | 4.54 | 3.94 | 3.76 | 4.60 | 2.25 | 8.38 | 3.70 | 13.4 |
| Be (ppm) | 1.81 | 1.79 | 1.63 | 2.05 | 1.57 | 1.87 | 1.81 | 2.05 | 1.94 | 1.76 | 2.46 | 2.50 | 1.68 | 2.41 | 1.72 |
| Sc (ppm) | 37.5 | 38.2 | 36.8 | 37.2 | 38.0 | 37.8 | 40.3 | 36.5 | 37.3 | 38.0 | 44.8 | 58.4 | 34.6 | 32.4 | 29.5 |
| V (ppm) | 237 | 239 | 224 | 225 | 227 | 219 | 238 | 203 | 202 | 193 | 216 | 272 | 195 | 187 | 188 |
| Cr (ppm) | 378 | 348 | 328 | 326 | 340 | 334 | 474 | 316 | 291 | 298 | 664 | 1770 | 422 | 355 | 284 |
| Co (ppm) | 40.1 | 45.2 | 40.7 | 38.4 | 37.6 | 39.8 | 40.9 | 43.8 | 62.8 | 55.7 | 113 | 43.7 | 195 | 64.2 | 201 |
| Ni (ppm) | 216 | 217 | 211 | 204 | 210 | 205 | 201 | 219 | 222 | 229 | 351 | 260 | 365 | 271 | 247 |
| Cu (ppm) | 114 | 141 | 112 | 112 | 112 | 114 | 121 | 112 | 112 | 112 | 137 | 154 | 126 | 109 | 117 |
| Zn (ppm) | 158 | 165 | 135 | 133 | 141 | 127 | 126 | 130 | 116 | 140 | 142 | 141 | 122 | 129 | 144 |
| Ga (ppm) | 38.3 | 38.8 | 39.8 | 39.7 | 39.6 | 39.3 | 39.0 | 38.1 | 39.3 | 39.0 | 39.4 | 50.0 | 37.1 | 38.7 | 35.8 |
| Rb (ppm) | 2.39 | 1.94 | 1.78 | 1.79 | 1.88 | 1.71 | 1.54 | 1.46 | 1.17 | 1.11 | 0.956 | 0.494 | 0.874 | 0.822 | 0.860 |
| Sr (ppm) | 33.0 | 20.3 | 18.8 | 19.6 | 20.0 | 18.7 | 15.8 | 14.3 | 12.5 | 10.2 | 13.5 | 6.09 | 5.51 | 5.52 | 11.8 |
| Zr (ppm) | 290 | 287 | 274 | 280 | 273 | 264 | 251 | 254 | 254 | 248 | 254 | 317 | 215 | 240 | 224 |
| Nb (ppm) | 58.0 | 57.3 | 52.2 | 53.4 | 51.6 | 48.4 | 43.4 | 42.3 | 42.3 | 40.8 | 41.4 | 51.8 | 36.1 | 40.7 | 38.5 |
| Mo (ppm) | 2.11 | 2.02 | 1.87 | 2.08 | 2.12 | 1.81 | 1.89 | 1.42 | 1.50 | 1.37 | 1.41 | 1.98 | 1.46 | 1.26 | 1.43 |
| Cs (ppm) | 0.270 | 0.288 | 0.274 | 0.324 | 0.312 | 0.307 | 0.251 | 0.260 | 0.208 | 0.209 | 0.185 | 0.098 | 0.136 | 0.140 | 0.141 |
| Ba (ppm) | 52.8 | 47.4 | 39.3 | 42.2 | 50.3 | 42.8 | 38.3 | 49.2 | 72.5 | 56.3 | 251 | 102 | 216 | 135 | 190 |
| Hf (ppm) | 7.11 | 7.07 | 6.92 | 6.99 | 7.19 | 6.70 | 6.45 | 6.63 | 6.05 | 6.25 | 6.75 | 8.39 | 5.51 | 6.45 | 5.40 |
| Ta (ppm) | 3.64 | 3.58 | 3.25 | 3.25 | 3.19 | 2.90 | 2.66 | 2.50 | 2.54 | 2.53 | 2.60 | 3.26 | 2.12 | 2.46 | 2.31 |
| Pb (ppm) | 6.56 | 6.66 | 5.20 | 5.50 | 4.96 | 4.80 | 4.53 | 4.06 | 5.54 | 3.86 | 5.31 | 4.12 | 4.66 | 5.04 | 4.23 |
| Th (ppm) | 7.21 | 6.51 | 6.24 | 6.48 | 6.14 | 5.84 | 5.43 | 5.10 | 5.17 | 4.98 | 5.46 | 6.39 | 4.12 | 4.94 | 4.81 |
| U (ppm) | 1.77 | 1.44 | 1.33 | 1.35 | 1.34 | 1.30 | 1.36 | 1.11 | 1.07 | 0.974 | 1.21 | 1.83 | 0.844 | 0.941 | 1.29 |
| TOC (%) | 1.53 | 1.32 | 0.749 | 0.723 | 0.779 | 0.435 | 0.321 | 0.256 | 0.238 | 0.237 | 0.217 | 0.189 | 0.186 | 0.166 | 0.100 |
| IC (%) | 0.270 | 0.139 | 0.118 | 0.277 | 0.026 | 0.174 | 0.113 | 0.099 | 0.094 | 0.062 | 0.043 | | | 0.009 | 0.012 |
| pH | 5.07 | 4.77 | 4.69 | 4.67 | 4.74 | 4.65 | 4.7 | 4.83 | 4.87 | 4.92 | 4.98 | 5.03 | 5.06 | 5.08 | 5.01 |
| Nb/Ta | 15.9 | 16.0 | 16.1 | 16.4 | 16.2 | 16.7 | 16.3 | 16.9 | 16.7 | 16.1 | 15.9 | 15.9 | 17.0 | 16.5 | 16.7 |
| Zr/Hf | 40.8 | 40.6 | 39.6 | 40.1 | 38.0 | 39.4 | 38.9 | 38.3 | 42.0 | 39.7 | 37.6 | 37.8 | 39.0 | 37.2 | 41.5 |
| Th/Nb | 0.124 | 0.114 | 0.120 | 0.121 | 0.119 | 0.121 | 0.125 | 0.121 | 0.122 | 0.122 | 0.132 | 0.123 | 0.114 | 0.121 | 0.125 |
| Th/Zr | 0.025 | 0.023 | 0.023 | 0.023 | 0.022 | 0.022 | 0.022 | 0.020 | 0.020 | 0.020 | 0.021 | 0.020 | 0.019 | 0.021 | 0.021 |
| $Th/TiO_2$ | 1.74 | 1.53 | 1.57 | 1.62 | 1.57 | 1.59 | 1.66 | 1.48 | 1.48 | 1.43 | 1.46 | 1.27 | 1.24 | 1.34 | 1.41 |
| $TiO_2/Zr$ | 0.014 | 0.015 | 0.014 | 0.014 | 0.014 | 0.014 | 0.013 | 0.014 | 0.014 | 0.014 | 0.015 | 0.016 | 0.015 | 0.015 | 0.015 |

| WC-16 | WC-17 | WC-18 | WC-19 | WC-20 | WC-21 | WC-22 | WC-23 | WC-24 | WC-25 | WC-26 | WC-27 | WC-28 | WC-29 | WC-30 | WC-31 | WC-31[a] |
|---|---|---|---|---|---|---|---|---|---|---|---|---|---|---|---|---|
| SP | SP | SP | SP | SP | SP | SP | SP | SP | SP | SP | SP | SP | SP | SP | SP | SP |
| 3.9 | 4.4 | 4.9 | 5.3 | 5.7 | 6.1 | 6.7 | 7.1 | 7.3 | 7.5 | 8.0 | 8.4 | 8.6 | 8.8 | 9.1 | 9.28 | |
| 32.6 | 33.3 | 35.8 | 33.4 | 33.2 | 32.4 | 34.5 | 34.8 | 33.3 | 33.9 | 33.6 | 33.2 | 32.5 | 34.4 | 34.5 | 34.7 | 34.7 |
| 3.97 | 3.78 | 3.13 | 3.61 | 3.65 | 3.53 | 3.57 | 3.84 | 3.94 | 3.77 | 3.65 | 3.80 | 3.86 | 3.83 | 3.73 | 3.66 | 3.65 |
| 26.8 | 27.0 | 29.3 | 28.1 | 27.5 | 27.5 | 28.2 | 28.4 | 27.2 | 27.2 | 27.0 | 26.6 | 26.0 | 27.1 | 27.3 | 27.3 | 27.3 |
| 22.2 | 22.3 | 17.2 | 20.2 | 21.1 | 20.1 | 19.1 | 18.6 | 21.3 | 21.9 | 21.4 | 22.6 | 24.2 | 21.5 | 21.1 | 21.1 | 21.1 |
| 0.31 | 0.19 | 0.13 | 0.23 | 0.23 | 1.82 | 0.47 | 0.32 | 0.29 | 0.19 | 0.28 | 0.21 | 0.29 | 0.19 | 0.23 | 0.20 | 0.22 |
| 0.24 | 0.23 | 0.20 | 0.34 | 0.24 | 0.25 | 0.19 | 0.25 | 0.19 | 0.16 | 0.18 | 0.16 | 0.17 | 0.14 | 0.14 | 0.13 | 0.13 |
| 0.37 | 0.42 | 0.47 | 0.29 | 0.40 | 0.33 | 0.39 | 0.46 | 0.46 | 0.50 | 0.50 | 0.45 | 0.45 | 0.47 | 0.59 | 0.55 | 0.55 |
| 0.01 | 0.01 | 0.01 | 0.01 | 0.01 | 0.01 | 0.01 | 0.02 | 0.03 | 0.01 | 0.01 | 0.01 | 0.02 | 0.03 | 0.01 | 0.01 | 0.02 |
| 0.03 | 0.01 | < 0.01 | < 0.01 | 0.01 | 0.01 | 0.01 | 0.01 | 0.01 | 0.01 | 0.01 | 0.02 | 0.01 | 0.02 | 0.02 | 0.02 | 0.02 |
| 0.01 | 0.01 | 0.01 | < 0.01 | 0.01 | 0.01 | < 0.01 | < 0.01 | 0.01 | < 0.01 | < 0.01 | < 0.01 | 0.01 | 0.01 | < 0.01 | < 0.01 | < 0.01 |
| 12.4 | 12.3 | 12.8 | 12.9 | 12.4 | 12.9 | 12.6 | 12.4 | 12.0 | 12.0 | 12.1 | 11.8 | 11.5 | 11.5 | 11.8 | 11.74 | 11.6 |
| 98.94 | 99.55 | 99.05 | 99.08 | 98.75 | 98.86 | 99.04 | 99.1 | 98.73 | 99.64 | 98.73 | 98.85 | 99.01 | 99.19 | 99.42 | 99.41 | 99.29 |
| 6.64 | 3.17 | 4.13 | 6.35 | 3.69 | 91.6 | 32.7 | 24.1 | 15.5 | 3.71 | 9.35 | 4.04 | 4.02 | 3.84 | 155 | 3.45 | 3.15 |
| 1.93 | 1.72 | 1.93 | 3.04 | 2.2 | 2.84 | 2.43 | 2.13 | 2.11 | 1.57 | 1.56 | 2.00 | 1.99 | 1.91 | 3.37 | 1.34 | 1.84 |
| 35.4 | 36.6 | 30.5 | 41.8 | 36.0 | 42.0 | 33.1 | 32.1 | 33.5 | 32.0 | 33.3 | 30.8 | 32.7 | 29.3 | 25.1 | 28.8 | 29.6 |
| 223 | 206 | 197 | 208 | 211 | 180 | 178 | 212 | 202 | 165 | 159 | 141 | 166 | 162 | 247 | 137 | 134 |
| 354 | 346 | 203 | 282 | 257 | 243 | 283 | 223 | 222 | 213 | 188 | 190 | 258 | 237 | 152 | 206 | 221 |
| 105 | 52.9 | 47.7 | 152 | 35.8 | 1830 | 603 | 407 | 334 | 46.4 | 88.3 | 69.2 | 78.2 | 64 | 45.4 | 53.6 | 66.4 |
| 207 | 196 | 168 | 348 | 190 | 631 | 286 | 258 | 224 | 182 | 231 | 171 | 168 | 142 | 101 | 119 | 109 |
| 125 | 122 | 98.7 | 125 | 111 | 371 | 220 | 163 | 159 | 89.3 | 93.6 | 79.9 | 93.6 | 77.2 | 63.8 | 72.4 | 69.5 |
| 127 | 109 | 100 | 133 | 116 | 272 | 161 | 212 | 159 | 128 | 126 | 109 | 115 | 112 | 110 | 138 | 94.0 |
| 40.7 | 38.5 | 33.5 | 37.1 | 38.1 | 38.4 | 37.5 | 38.2 | 39.8 | 38.1 | 36.8 | 37.7 | 41.2 | 40.5 | 34.2 | 36.9 | 36.2 |
| 1.03 | 0.493 | 1.30 | 0.610 | 1.72 | 0.767 | 0.904 | 1.07 | 1.09 | 0.656 | 0.845 | 0.710 | 1.61 | 1.17 | 2.13 | 0.872 | 0.732 |
| 51.4 | 34.4 | 24.0 | 6.35 | 6.90 | 11.6 | 40.7 | 119 | 48.9 | 28.6 | 22.9 | 33.8 | 46.2 | 38.7 | 35.5 | 34.6 | 33.1 |

**Table 2** (*continued*)

| WC-16 | WC-17 | WC-18 | WC-19 | WC-20 | WC-21 | WC-22 | WC-23 | WC-24 | WC-25 | WC-26 | WC-27 | WC-28 | WC-29 | WC-30 | WC-31 | WC-31[a] |
|---|---|---|---|---|---|---|---|---|---|---|---|---|---|---|---|---|
| 272 | 260 | 209 | 234 | 236 | 219 | 225 | 242 | 262 | 248 | 242 | 249 | 263 | 260 | 265 | 236 | 234 |
| 52.1 | 49.6 | 36.8 | 38.9 | 39.2 | 36.9 | 37.3 | 43.9 | 47.1 | 47.1 | 45.5 | 46.0 | 47.5 | 47.7 | 39.8 | 43.4 | 47.3 |
| 1.38 | 1.62 | 0.768 | 1.03 | 1.16 | 1.94 | 1.07 | 0.909 | 0.880 | 0.977 | 0.802 | 1.10 | 0.926 | 0.952 | 1.02 | 1.04 | 1.19 |
| 0.165 | 0.180 | 0.242 | 0.109 | 0.232 | 0.161 | 0.198 | 0.225 | 0.208 | 0.193 | 0.253 | 0.251 | 0.247 | 0.266 | 0.412 | 0.264 | 0.228 |
| 235 | 128 | 99 | 211 | 159 | 1100 | 515 | 684 | 545 | 154 | 156 | 196 | 246 | 193 | 118 | 176 | 178 |
| 7.01 | 6.65 | 5.08 | 6.23 | 5.76 | 6.01 | 5.63 | 6.11 | 6.99 | 6.23 | 5.65 | 6.36 | 6.77 | 6.41 | 6.83 | 5.43 | 6.05 |
| 3.21 | 3.09 | 2.12 | 2.42 | 2.39 | 2.23 | 2.27 | 2.48 | 2.80 | 2.77 | 2.69 | 2.72 | 2.85 | 2.84 | 2.46 | 2.48 | 2.68 |
| 4.06 | 4.48 | 2.60 | 3.78 | 3.83 | 4.81 | 3.59 | 3.93 | 4.57 | 3.67 | 3.44 | 4.95 | 4.08 | 4.48 | 6.63 | 3.37 | 3.37 |
| 5.97 | 5.86 | 4.30 | 4.48 | 4.58 | 4.42 | 4.51 | 5.02 | 5.76 | 5.45 | 5.19 | 5.24 | 5.68 | 5.50 | 7.78 | 4.88 | 5.29 |
| 1.42 | 1.35 | 1.06 | 1.21 | 0.998 | 1.19 | 2.19 | 2.79 | 2.20 | 1.08 | 0.885 | 0.822 | 0.868 | 0.913 | 4.92 | 0.884 | 0.940 |
| 0.128 | 0.243 | 0.095 | 0.084 | 0.144 | 0.111 | 0.103 | 0.120 | 0.112 | 0.173 | 0.095 | 0.099 | 0.097 | 0.103 | 0.167 | 0.113 | |
| 0.005 | | 0.011 | | | | | | | | | | | | | | |
| 4.96 | 4.92 | 4.81 | 4.84 | 4.74 | 4.81 | 4.71 | 4.75 | 4.75 | 4.77 | 4.81 | 4.77 | 4.75 | 4.74 | 4.79 | 4.85 | |
| 16.2 | 16.1 | 17.4 | 16.1 | 16.4 | 16.5 | 16.4 | 17.7 | 16.8 | 17.0 | 16.9 | 16.9 | 16.7 | 16.8 | 16.2 | 17.5 | 17.6 |
| 38.8 | 39.1 | 41.1 | 37.6 | 41.0 | 36.4 | 40.0 | 39.6 | 37.5 | 39.8 | 42.8 | 39.2 | 38.8 | 40.6 | 38.8 | 43.5 | 38.7 |
| 0.115 | 0.118 | 0.117 | 0.115 | 0.117 | 0.120 | 0.121 | 0.114 | 0.122 | 0.116 | 0.114 | 0.114 | 0.120 | 0.115 | 0.195 | 0.112 | 0.112 |
| 0.022 | 0.023 | 0.021 | 0.019 | 0.019 | 0.020 | 0.020 | 0.021 | 0.022 | 0.022 | 0.021 | 0.021 | 0.022 | 0.021 | 0.029 | 0.021 | 0.023 |
| 1.50 | 1.55 | 1.37 | 1.24 | 1.25 | 1.25 | 1.26 | 1.31 | 1.46 | 1.45 | 1.42 | 1.38 | 1.47 | 1.44 | 2.09 | 1.33 | 1.45 |
| 0.015 | 0.015 | 0.015 | 0.015 | 0.015 | 0.016 | 0.016 | 0.016 | 0.015 | 0.015 | 0.015 | 0.015 | 0.015 | 0.015 | 0.014 | 0.016 | 0.016 |

| WC-32 | WC-33 | WC-34 | WC-35 | WC-36 | WC-37 | WC-38 | WC-39 | WC-40 | WC-41 | WC-42 | WC-43 | WC-44 | WC-45 | WC-46 | WC-47 | WC-48 |
|---|---|---|---|---|---|---|---|---|---|---|---|---|---|---|---|---|
| SP | SP | SP | SP | SP | SP | SP | SP | SP | SP | SP | SP | SP | SP | SP | SP | SP |
| 9.56 | 9.84 | 10.12 | 10.4 | 10.68 | 10.96 | 11.24 | 11.52 | 11.8 | 12.08 | 12.36 | 12.64 | 12.92 | 13.2 | 13.48 | 13.76 | 14.04 |
| 34.7 | 34.8 | 34.2 | 33.7 | 34.5 | 34.6 | 34.6 | 33.6 | 34.4 | 34.1 | 34.9 | 35.6 | 34.0 | 34.1 | 35.0 | 34.0 | 35.5 |
| 3.82 | 3.49 | 3.64 | 3.76 | 3.59 | 3.54 | 3.53 | 3.56 | 3.53 | 3.54 | 3.66 | 3.38 | 3.83 | 3.73 | 3.45 | 3.71 | 3.18 |
| 27.2 | 27.4 | 26.9 | 26.4 | 27.0 | 27.0 | 26.8 | 26.2 | 26.6 | 26.9 | 26.5 | 26.9 | 26.2 | 26.5 | 26.6 | 26.1 | 26.5 |
| 21.2 | 20.6 | 21.9 | 23.0 | 21.7 | 21.6 | 20.7 | 22.0 | 21.5 | 21.4 | 21.2 | 20.2 | 22.1 | 21.5 | 19.7 | 21.3 | 19.7 |
| 0.24 | 0.28 | 0.38 | 0.40 | 0.26 | 0.27 | 0.28 | 0.33 | 0.27 | 0.37 | 0.28 | 0.26 | 0.57 | 0.26 | 0.28 | 0.30 | 0.33 |
| 0.12 | 0.12 | 0.12 | 0.14 | 0.10 | 0.10 | 0.21 | 0.36 | 0.14 | 0.21 | 0.09 | 0.08 | 0.15 | 0.16 | 0.26 | 0.37 | 0.36 |
| 0.58 | 0.68 | 0.62 | 0.6 | 0.68 | 0.62 | 0.8 | 0.99 | 0.74 | 0.73 | 0.93 | 0.76 | 0.63 | 0.6 | 0.78 | 0.85 | 1.22 |
| 0.02 | 0.02 | 0.03 | 0.04 | 0.02 | 0.02 | 0.05 | 0.06 | 0.08 | 0.06 | 0.13 | 0.14 | 0.13 | 0.09 | 0.14 | 0.14 | 0.17 |
| 0.05 | 0.02 | 0.03 | 0.02 | 0.01 | 0.01 | 0.02 | 0.02 | 0.02 | 0.02 | 0.03 | 0.01 | 0.02 | 0.01 | 0.01 | 0.02 | 0.04 |
| < 0.01 | < 0.01 | < 0.01 | < 0.01 | < 0.01 | < 0.01 | < 0.01 | < 0.01 | < 0.01 | < 0.01 | < 0.01 | < 0.01 | 0.01 | 0.01 | < 0.01 | 0.01 | < 0.01 |
| 11.7 | 12.1 | 11.7 | 11.5 | 12.0 | 12.2 | 12.3 | 12.4 | 12.1 | 12.2 | 12.0 | 11.7 | 11.8 | 11.9 | 12.6 | 12.2 | 12.6 |
| 99.62 | 99.53 | 99.5 | 99.56 | 99.89 | 99.91 | 99.32 | 99.48 | 99.35 | 99.52 | 99.76 | 99.06 | 99.4 | 98.81 | 98.79 | 99.03 | 99.57 |
| 3.95 | 3.46 | 3.82 | 3.51 | 3.22 | 3.09 | 3.34 | 3.57 | 3.84 | 6.29 | 3.63 | 4.60 | 6.34 | 4.65 | 4.51 | 5.56 | 4.15 |
| 1.86 | 1.63 | 1.6 | 1.54 | 1.87 | 2.13 | 2.12 | 3.39 | 2.11 | 2.26 | 1.91 | 1.69 | 2.53 | 2.37 | 3.21 | 4.43 | 4.50 |
| 29.6 | 30.2 | 29.9 | 30.2 | 34.3 | 33.1 | 35.9 | 39.4 | 36.8 | 36.6 | 35.0 | 31.0 | 34.5 | 35.4 | 36.4 | 36.8 | 37.6 |
| 137 | 125 | 136 | 181 | 134 | 124 | 153 | 186 | 150 | 160 | 140 | 139 | 162 | 157 | 159 | 191 | 185 |
| 200 | 149 | 162 | 226 | 151 | 143 | 186 | 274 | 216 | 216 | 162 | 254 | 238 | 233 | 216 | 284 | 279 |
| 87.0 | 80.2 | 96.4 | 102 | 120 | 92.4 | 89.9 | 106 | 111 | 154 | 79.1 | 74.1 | 171 | 86.0 | 78.5 | 109 | 104 |
| 119 | 106 | 122 | 130 | 121 | 116 | 173 | 217 | 156 | 185 | 124 | 140 | 202 | 175 | 243 | 292 | 229 |
| 78.9 | 91.9 | 97.9 | 98.7 | 106 | 100 | 118 | 137 | 113 | 127 | 109 | 97.0 | 134 | 116 | 129 | 146 | 141 |
| 135 | 121 | 143 | 130 | 125 | 118 | 129 | 131 | 147 | 146 | 157 | 107 | 147 | 151 | 170 | 171 | 203 |
| 39.1 | 36.3 | 38.2 | 37.6 | 38.9 | 36.5 | 35.9 | 37.9 | 37.3 | 37.2 | 37.3 | 34.2 | 37.7 | 37.9 | 34.6 | 36.2 | 33.1 |
| 0.661 | 0.804 | 0.793 | 0.68 | 0.598 | 0.738 | 0.753 | 0.782 | 0.956 | 1.06 | 0.841 | 0.89 | 2.14 | 1.12 | 0.909 | 0.759 | 0.692 |
| 48.3 | 31.9 | 33.5 | 40.7 | 7.12 | 5.40 | 15.5 | 18.1 | 15.0 | 28.1 | 11.5 | 11.6 | 30.3 | 14.2 | 16.5 | 24.5 | 15.7 |
| 252 | 233 | 238 | 243 | 230 | 224 | 240 | 253 | 238 | 240 | 234 | 217 | 260 | 255 | 230 | 239 | 206 |
| 45.8 | 42.7 | 42.3 | 42.8 | 40.9 | 39.1 | 43.6 | 47.4 | 40.3 | 42.6 | 38.5 | 35.6 | 44.5 | 43.4 | 39.7 | 40.7 | 35.9 |
| 1.22 | 0.944 | 1.09 | 0.982 | 0.863 | 0.771 | 1.01 | 1.25 | 2.01 | 1.34 | 1.45 | 1.29 | 1.18 | 1.40 | 1.13 | 1.20 | 1.13 |
| 0.230 | 0.235 | 0.206 | 0.203 | 0.187 | 0.188 | 0.138 | 0.136 | 0.188 | 0.171 | 0.199 | 0.122 | 0.221 | 0.170 | 0.115 | 0.149 | 0.104 |
| 232 | 184 | 239 | 322 | 82.8 | 74.0 | 123 | 177 | 133 | 215 | 85.4 | 142 | 347 | 137 | 146 | 186 | 136 |
| 6.04 | 5.72 | 6.08 | 6.16 | 5.38 | 5.23 | 6.43 | 6.73 | 6.33 | 6.18 | 6.41 | 6.04 | 6.94 | 6.49 | 5.77 | 6.11 | 5.28 |
| 2.72 | 2.36 | 2.51 | 2.58 | 2.34 | 2.33 | 2.80 | 2.98 | 2.64 | 2.65 | 2.40 | 2.20 | 2.89 | 2.78 | 2.36 | 2.43 | 2.12 |
| 4.20 | 3.76 | 4.08 | 4.33 | 3.30 | 2.88 | 3.22 | 3.42 | 3.99 | 4.31 | 2.53 | 2.99 | 4.62 | 3.91 | 2.86 | 3.13 | 3.55 |
| 5.30 | 4.79 | 5.07 | 4.85 | 4.76 | 4.5 | 5.42 | 5.97 | 4.84 | 5.11 | 4.33 | 4.11 | 5.50 | 5.11 | 4.29 | 4.79 | 3.97 |
| 0.951 | 1.06 | 1.08 | 0.877 | 0.849 | 0.771 | 1.08 | 1.32 | 1.18 | 1.20 | 1.31 | 0.719 | 1.11 | 0.958 | 1.00 | 1.28 | 1.10 |
| 0.093 | 0.081 | 0.123 | 0.201 | 0.137 | 0.073 | 0.073 | 0.244 | 0.185 | 0.205 | 0.197 | 0.173 | 0.182 | 0.170 | 0.136 | 0.139 | 0.153 |
| 4.82 | 4.87 | 4.94 | 4.93 | 4.93 | 4.97 | 5.00 | 5.00 | 5.01 | 4.98 | 5.24 | 5.43 | 5.29 | 5.28 | 5.47 | 5.58 | 5.55 |
| 16.8 | 18.1 | 16.9 | 16.6 | 17.5 | 16.8 | 15.6 | 15.9 | 15.3 | 16.1 | 16.0 | 16.2 | 15.4 | 15.6 | 16.8 | 16.7 | 16.9 |
| 41.7 | 40.7 | 39.1 | 39.4 | 42.8 | 42.8 | 37.3 | 37.6 | 37.6 | 38.8 | 36.5 | 35.9 | 37.5 | 39.3 | 39.9 | 39.1 | 39.0 |
| 0.116 | 0.112 | 0.120 | 0.113 | 0.116 | 0.115 | 0.124 | 0.126 | 0.120 | 0.120 | 0.112 | 0.115 | 0.124 | 0.118 | 0.108 | 0.118 | 0.111 |
| 0.021 | 0.021 | 0.021 | 0.020 | 0.021 | 0.020 | 0.023 | 0.024 | 0.020 | 0.021 | 0.019 | 0.019 | 0.021 | 0.020 | 0.019 | 0.020 | 0.019 |
| 1.39 | 1.37 | 1.39 | 1.29 | 1.33 | 1.27 | 1.54 | 1.68 | 1.37 | 1.44 | 1.18 | 1.22 | 1.44 | 1.37 | 1.24 | 1.29 | 1.25 |
| 0.015 | 0.015 | 0.015 | 0.015 | 0.016 | 0.016 | 0.015 | 0.014 | 0.015 | 0.015 | 0.016 | 0.016 | 0.015 | 0.015 | 0.015 | 0.016 | 0.015 |

| WC-49 | WC-50 | WC-51 | WC-52 | WC-53 | WC-54 | WC-55 | WC-56 | WC-57 | WC-58 | GSS-4 | GSS-4[b] | GSS-7 | GSS-7[b] | GSR-1 | GSR-1[b] |
|---|---|---|---|---|---|---|---|---|---|---|---|---|---|---|---|
| SP | SP | SP | SP | SWB[d] | Basalt | Basalt | Basalt | Basalt | Basalt | Soil | Soil | Soil | Soil | Granite | Granite |
| 14.32 | 14.6 | 14.88 | 15.16 | 15.28 | 15.83 | 16.43 | 17.43 | 18.73 | 19.73 | | | | | | |
| 33.4 | 34.7 | 35.6 | 37.5 | 42.7 | 51.4 | 51.4 | 50.2 | 51.1 | 51.1 | 50.8 | 50.9 | 32.7 | 32.7 | 72.9 | 72.8 |
| 3.50 | 3.32 | 3.72 | 3.02 | 2.68 | 1.96 | 1.93 | 1.90 | 1.93 | 1.93 | 1.78 | | 3.40 | | 0.28 | 0.29 |
| 26.1 | 25.1 | 24.1 | 24.9 | 18.8 | 14.2 | 14.1 | 13.9 | 14.1 | 14.1 | 23.6 | 23.5 | 29.4 | 29.3 | 13.4 | 13.4 |

**Table 2** (*continued*)

| WC-49 | WC-50 | WC-51 | WC-52 | WC-53 | WC-54 | WC-55 | WC-56 | WC-57 | WC-58 | GSS-4 | GSS-4[b] | GSS-7 | GSS-7[b] | GSR-1 | GSR-1[b] |
|---|---|---|---|---|---|---|---|---|---|---|---|---|---|---|---|
| 21.1 | 20.9 | 20.5 | 18.1 | 14.8 | 11.0 | 11.3 | 11.7 | 11.5 | 11.5 | 10.1 | 10.3 | 18.8 | 18.8 | 2.15 | 2.14 |
| 0.27 | 0.44 | 0.14 | 0.28 | 0.12 | 0.12 | 0.17 | 0.13 | 0.15 | 0.15 | 0.19 | | 0.24 | | 0.06 | 0.06 |
| 0.56 | 0.62 | 0.62 | 0.42 | 0.57 | 0.32 | 0.33 | 0.32 | 0.32 | 0.32 | 0.15 | | 0.26 | | 0.09 | 0.14 |
| 0.80 | 0.87 | 1.76 | 2.00 | 5.35 | 6.8 | 7.44 | 7.53 | 7.39 | 7.40 | 0.46 | 0.49 | 0.22 | 0.26 | 0.40 | 0.42 |
| 0.16 | 0.20 | 0.30 | 0.33 | 4.34 | 8.67 | 8.45 | 8.46 | 8.71 | 8.68 | 0.23 | 0.26 | 0.13 | 0.16 | 1.53 | 1.55 |
| 0.03 | 0.04 | 0.03 | 0.04 | 0.96 | 3.08 | 3.20 | 2.84 | 2.96 | 2.93 | 0.08 | 0.11 | 0.05 | 0.07 | 3.07 | 3.13 |
| 0.01 | 0.01 | 0.01 | 0.01 | 0.24 | 0.78 | 1.02 | 0.64 | 0.68 | 0.68 | 1.04 | 1.03 | 0.19 | 0.20 | 5.00 | 5.01 |
| 12.89 | 12.61 | 12.24 | 12.31 | 9.22 | 1.14 | 0.66 | 1.68 | 0.63 | 0.57 | 10.5 | | 13.7 | | 0.59 | |
| 98.82 | 98.81 | 99.02 | 98.91 | 99.78 | 99.47 | 100 | 99.3 | 99.47 | 99.36 | 98.93 | | 99.09 | | 99.47 | |
| 6.44 | 4.88 | 4.84 | 5.00 | 40.8 | 5.36 | 5.64 | 5.23 | 5.56 | 5.77 | 58.6 | 56.0 | 18.9 | 19.5 | 126 | 131 |
| 6.28 | 6.52 | 6.18 | 5.38 | 2.72 | 1.53 | 1.26 | 1.18 | 1.23 | 1.23 | 1.26 | 1.85 | 2.96 | 2.80 | 14.9 | 12.4 |
| 42.5 | 38.9 | 35.1 | 27.7 | 27.1 | 20.3 | 18.8 | 18.3 | 19.5 | 19.0 | 18.6 | 20.0 | 25.4 | 28.0 | 7.31 | 6.10 |
| 240 | 234 | 232 | 201 | 187 | 160 | 150 | 148 | 153 | 148 | 227 | 247 | 229 | 245 | 25.3 | 24.0 |
| 417 | 331 | 376 | 258 | 349 | 210 | 215 | 200 | 213 | 206 | 354 | 370 | 388 | 410 | 1.93 | 3.60 |
| 160 | 135 | 59.8 | 70.3 | 49.8 | 61.1 | 62.3 | 47.3 | 58.5 | 70.5 | 22.2 | 22.0 | 95.4 | 97.0 | 2.85 | 3.40 |
| 497 | 506 | 553 | 411 | 589 | 150 | 149 | 142 | 143 | 141 | 60.3 | 64.0 | 258 | 276 | 3.46 | 2.30 |
| 185 | 191 | 189 | 139 | 192 | 63.4 | 62.7 | 60.1 | 66.8 | 62.6 | 44.9 | 40.0 | 104 | 97.0 | 3.17 | 3.20 |
| 173 | 196 | 262 | 213 | 535 | 124 | 112 | 111 | 116 | 109 | 195 | 210 | 142 | 142 | 29.0 | 28.0 |
| 36.6 | 37.2 | 36.0 | 31.2 | 26.8 | 20.1 | 18.7 | 19.1 | 19.7 | 19.1 | 31.0 | 31.0 | 38.1 | 39.0 | 19.1 | 19.0 |
| 0.841 | 1.19 | 0.750 | 0.922 | 4.04 | 19.0 | 25.2 | 12.9 | 16.7 | 15.8 | 74.7 | 75.0 | 16.0 | 16.0 | 346 | 466 |
| 17.6 | 29.4 | 79.7 | 27.0 | 115 | 423 | 386 | 394 | 431 | 417 | 89.4 | 77.0 | 30.6 | 26.0 | 118 | 106 |
| 229 | 220 | 256 | 197 | 178 | 136 | 131 | 126 | 137 | 130 | 456 | 500 | 326 | 318 | 171 | 167 |
| 39.4 | 38.0 | 45.2 | 35.7 | 31.4 | 24.7 | 23.9 | 22.9 | 24.4 | 22.4 | 36.6 | 38.0 | 61.9 | 64.0 | 40.3 | 40.0 |
| 1.25 | 1.26 | 1.08 | 0.943 | 0.605 | 0.644 | 1.03 | 0.697 | 1.12 | 1.14 | 2.89 | 2.60 | 3.03 | 2.90 | 3.39 | 3.50 |
| 0.107 | 0.224 | 0.086 | 0.114 | 0.326 | 0.516 | 0.268 | 0.389 | 0.306 | 0.316 | 19.7 | 21.4 | 2.32 | 2.70 | 33.0 | 38.4 |
| 290 | 357 | 357 | 300 | 451 | 324 | 310 | 303 | 296 | 279 | 224 | 213 | 201 | 188 | 342 | 343 |
| 5.71 | 5.99 | 6.75 | 4.76 | 4.25 | 3.33 | 3.19 | 3.07 | 3.28 | 3.16 | 11.8 | 8.10 | 7.61 | 7.70 | 5.48 | 6.30 |
| 2.40 | 2.31 | 2.73 | 2.06 | 1.90 | 1.45 | 1.37 | 1.42 | 1.47 | 1.45 | 2.90 | 3.10 | 3.80 | 3.90 | 6.07 | 7.20 |
| 4.02 | 2.90 | 2.56 | 2.18 | 2.55 | 1.66 | 1.55 | 1.76 | 1.30 | 1.34 | 64.7 | 58.0 | 12.1 | 14.0 | 31.8 | 31.0 |
| 4.78 | 4.40 | 5.11 | 3.93 | 3.50 | 2.70 | 2.56 | 2.51 | 2.71 | 2.65 | 24.6 | 27.0 | 8.33 | 9.10 | 48.9 | 54.0 |
| 1.25 | 1.16 | 0.957 | 0.691 | 0.850 | 0.602 | 0.567 | 1.02 | 0.668 | 0.596 | 6.94 | 6.70 | 2.11 | 2.20 | 18.0 | 18.8 |
| 0.164 | 0.207 | 0.199 | 0.172 | 0.136 | | | | | | | | | | | |
| | | | | | | | | | | | | | | | |
| 5.95 | 6.05 | 6.07 | 6.05 | 5.84 | | | | | | | | | | | |
| 16.4 | 16.5 | 16.6 | 17.3 | 16.5 | 17.0 | 17.4 | 16.1 | 16.6 | 15.4 | 12.6 | | 16.3 | | 6.64 | |
| 40.1 | 36.7 | 37.9 | 41.4 | 41.9 | 40.8 | 41.1 | 41.0 | 41.8 | 41.1 | 38.6 | | 42.8 | | 31.2 | |
| 0.121 | 0.116 | 0.113 | 0.110 | 0.111 | 0.109 | 0.107 | 0.110 | 0.111 | 0.118 | 0.672 | | 0.135 | | 1.21 | |
| 0.021 | 0.020 | 0.020 | 0.020 | 0.020 | 0.020 | 0.020 | 0.020 | 0.020 | 0.020 | | | | | | |
| 1.37 | 1.33 | 1.37 | 1.30 | 1.31 | 1.38 | 1.33 | 1.32 | 1.40 | 1.37 | | | | | | |
| 0.015 | 0.015 | 0.015 | 0.015 | 0.015 | 0.014 | 0.015 | 0.015 | 0.014 | 0.015 | | | | | | |

[a] WC-31[a] represents the repeated analytical results of sample WC-31.

[b] The recommended values for GSS-4, GSS-7 and GSR-1 (Data after http://www.ncrm.org.cn/English/Home/Index.aspx).

[c] SP = Saprolite.

[d] SWB = semi-weathered basalt. Blank stands for below detection limit or not detected.

(e.g., WC-10 and WC-30) display gypsum XRD diffraction peaks.

SEM-EDS analyses indicate that Fe-Ti oxides are common in the soil and saprolite samples. These Fe-Ti oxides are irregularly-shaped and with different sizes (max: 15 μm × 5 μm) (Fig. 3a and g). Apart from Fe, Ti and O, some Fe-Ti oxides grains also contain Cr, Cu and Zn. Aluminum oxides/hydroxides grains are common in the samples near the soil-saprolite interface (Fig. 3b), and are identified as gibbsite by XRD analyses. In the Fe-Mn-rich grains (up to 20 μm × 10 μm), distinct Ba peaks were detected (Fig. 3e). Irregular massive aggregates of Cu-Zn-rich grains (size: 5 μm × 3 μm), containing mainly O, Si, Al, Fe, Cu and Zn (Fig. 3c), were also indentified in some saprolite samples. Some samples (e.g., WC-23) in the middle and upper part of the weathering profile contain irregular massive aggregates of carbonate mineral grains (size: 6 μm × 5 μm), whose major components are Ca, O, C and Mg (Fig. 3f). Tiny Ce-bearing mineral grains were identified in most Ce-rich soil samples (i.e., WC-28 and WC-36). These grains (2–4 μm × 1–2 μm) are mainly irregularly massive or spherical in shape, and contain mainly O, Si, Al, Ce, Fe and Ti (Si, Al, Fe and Ti in the spectrum may have been influenced by the secondary clay minerals or Fe-Ti oxides around the analyzed grains). These Ce-bearing mineral grains are possibly cerianite (Fig. 3h and i). Soil samples from near the rock-regolith interface contain REE-bearing secondary phosphate grains (4–6 μm × 2–3 μm) (Fig. 3j and k), which are often of needle/columnar shape or as massive aggregates. These phosphate grains contain mainly La, Nd, Y, P and Ca, and Cu and Zn peaks. Similar to the Ce-bearing grains, the Si,

Al, Fe and Ti in the spectra may also have been affected by the background compositions. Soil samples from near the rock-regolith interface also contain smaller Ni-rich phosphate mineral grains, with grain sizes being 2.5 μm × 2 μm (e.g., WC-52; Fig. 3l).

### 4.2. Major elements

Soil and saprolite samples from the Wenchang weathering profile contain relatively high $Al_2O_3$ (18.8–32.3%), $Fe_2O_3$ (14.8–28.5%) and $TiO_2$ (2.68–5.03%) contents, which are one to three times higher than that of the fresh basalt samples. The maximum concentrations of these oxides occur at the soil-saprolite interface ($\sim$2.4 m deep; Fig. 4). In contrast, the CaO (0.01–0.33%), $Na_2O$ (0.01–0.07%), $K_2O$ (0.01–0.04%) and MgO contents are distinctly lower than those of the fresh basalt, with some samples even have their $K_2O$ and $Na_2O$ contents below the XRF detection limit (< 0.01%). The $SiO_2$ contents (13.3–42.7%) decreases progressively from the bottom to the top of the profile, and are also markedly lower than the fresh basalts ($\sim$51%). Compared with the consistent $P_2O_5$ content (0.32%) in the fresh basalt samples, those of the soil and saprolite samples are more variable (0.08–0.64%), with enrichment peaks occur in the samples around the soil-saprolite and rock-regolith interfaces. The MnO contents are fairly consistent (0.13–0.57%) across the profile, and are slightly higher than those of the basalt (average: 0.14%), whose maximum content (1.82%) occurs at 6.1 m deep. Loss on ignition (LOI) of the soil and saprolite
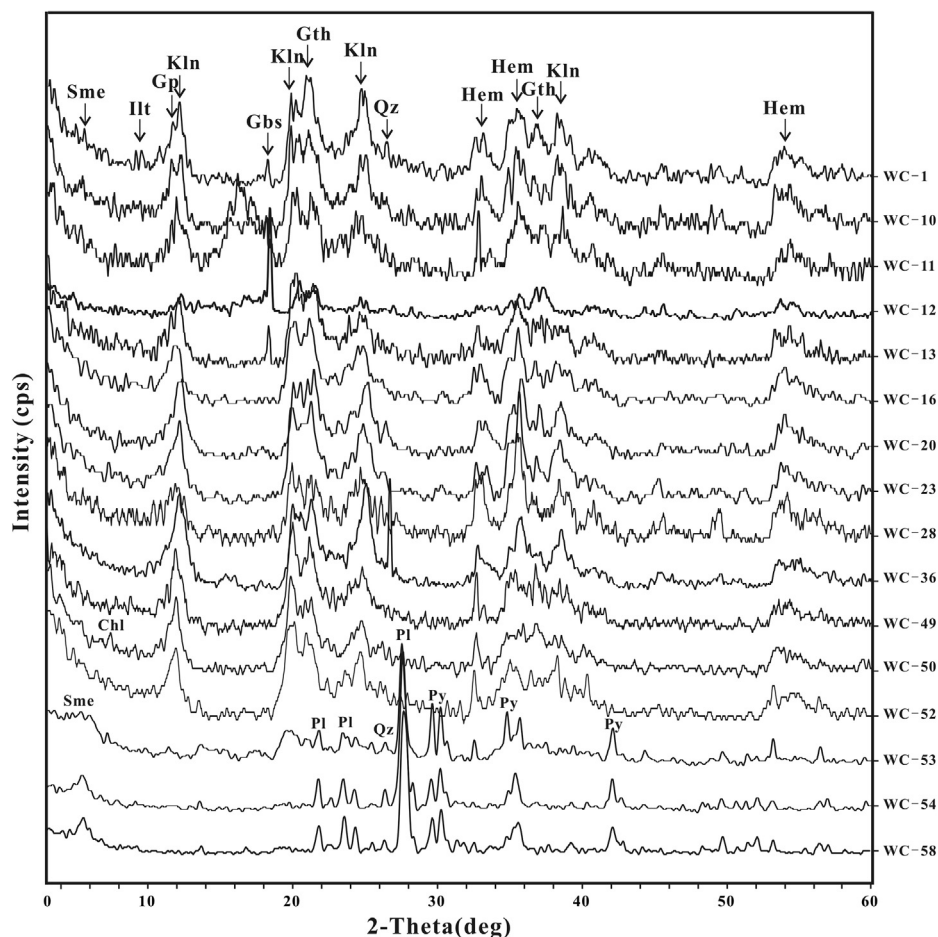
**Fig. 2.** XRD spectra of representative samples from the Wenchang basalt weathering profile, where Sme = Smectite, Chl = Chlorite, Ilt = Illite, Gp = Gypsum, Kln = Kaolinite, Gbs = Gibbsite, Gth = Goethite, Qz = Quartz, Hem = Hematite, Pl = Plagioclase, Py = Pyroxene.

samples (9.22–19.2%) decreases from the top to the bottom of the profile, with the highest value (19.2%) occurs at the soil-saprolite interface. The sample near the soil-saprolite interface (WC-12), which contains mainly gibbsite and Fe oxides/hydroxides, exhibits enrichment peaks of $Al_2O_3$, $Fe_2O_3$, $TiO_2$ and LOI, and depletion peak of $SiO_2$ (Table 2; Fig. 4).

### 4.3. Trace elements

The trace elements analyzed can be grouped into four categories based on elemental properties and the vertical composition variations across the weathering profile (Fig. 4):

(1) Alkali and alkaline earth metals (e.g., Rb, Sr, Ba, Li and Be). The Rb and Sr concentrations in the soil and saprolite samples are distinctly lowered than those in the basalt samples. There is no clear Rb variation pattern across the profile, whereas there are slight Sr enrichment peaks at 3.9 m and 7.1 m deep. Overall, Ba contents in the soil and saprolite samples are also lower than those in the basalt samples, with distinct enrichment (up to 1100 ppm) occurs at 6.1 m deep. Lithium concentrations in the soil and saprolite samples are also slightly lower than those in the basalt samples, but distinct enrichments occur at 6.1 m and 9.1 m deep, as well as near the rock-regolith interface. In contrast, Be concentrations in the soil and saprolite are slightly higher than those of the basalt. Mild Be enrichment is also found near the rock-regolith interface, where Be concentration can be up to 6.52 ppm.

(2) Redox sensitive elements (e.g., Co, Cr and U). These elements are variably enriched at different depths of the weathering profile.

Cobalt concentrations show variation trend very similar to that of MnO, and with similar enrichment peak (WC-21, 1830 ppm) at 6.1 m deep. Both Cr and U concentrations are slightly higher in the soil and saprolite than in the basalt. Chromium concentration shows a marked enrichment peak near the soil-saprolite interface (WC-12: 1770 ppm). Uranium concentrations decrease progressively from the top of the profile, and exhibit mild enrichments at 7.1 m (WC-23, 2.79 ppm) and 9.1 m (WC-30, 4.92 ppm) deep.

(3) Immobile elements (e.g., Zr, Hf, Nb, Ta and Th). These elements are distinctly more concentrated in the soil and saprolite samples than in the basalt samples, displaying similar downward decreasing variation trend, and slight enrichment near the soil-saprolite interface. There is no obvious vertical variation trend for the Nb/Ta and Zr/Hf ratio, similar to those in the basaltic parent rocks (Table 2).

(4) Transition metals (e.g., Cu, Zn, Ni, Sc and V). Copper, Zn, Ni and Sc concentrations in the soil and saprolite samples are similar or higher than those in the basalt. Copper and Ni exhibit clear enrichment peaks at 2.4 m and 6.1 m deep and near the rock-regolith interface. Zinc are enriched at 6.1 m deep and near the rock-regolith interface (WC-53, 689 ppm), whilst Sc is more enriched near the soil-saprolite interface (WC-12, 58.4 ppm). The V enrichment peaks occur at 9.1 m and near the soil-saprolite and rock-regolith interfaces.

### 4.4. Soil pH values and carbon contents

Total organic carbon (TOC) contents of the soil and saprolite samples range from 0.084% to 1.533%, of which the maximum value occurs

in the uppermost part of the profile, and decreases steadily until it reaches a minimum near the soil-saprolite interface (2.4 m deep), and then stays constantly (about 0.018%) in the saprolite horizon (Fig. 4). The calculated inorganic carbon (IC) contents ranges from 0.005% to 0.27%, which are generally depleted along depth in the soil horizon (Table 2). The pH values of soil and saprolite samples range from 4.65 to 6.07. From the top to the middle part of soil horizon, pH values decrease to a minimum (4.65, at 1.1 m deep), then rise across soil-saprolite interface to 5.08 (at 3.1 m deep), and then drop again to 4.74 (at 8.8 m deep). From that downward, pH values increase until they reach the maximum (6.07) near the rock-regolith interface (Fig. 4).

## 4.5. Mass balance calculation

Mass balance calculations based on Nb as reference element indicate that: (1) Almost all elements (except Ta and Th) in the upper soil samples are leached, and these leached elements are reconcentrated in the middle-lower parts of the profile and along the rock-regolith interface; (2) Except for immobile elements such as Al, Fe, Ti, Nb, Ta, Zr, Hf and Ga, the concentrations of most elements are positively correlated with their mass-transfer coefficients, and higher element contents (Fig. 4) generally imply relatively lower net loss or higher net gain (Fig. 5).

Ma et al. (2007) found that the enrichments or peaks of $\tau_{Th,j}$ of Al, Mn, Co, Ce and U (at about 3 m deep) in $\tau_{Th,j}$-depth profiles, as well as REE (except Ce) enrichment and TOC depletion (at about 3.5 m deep),
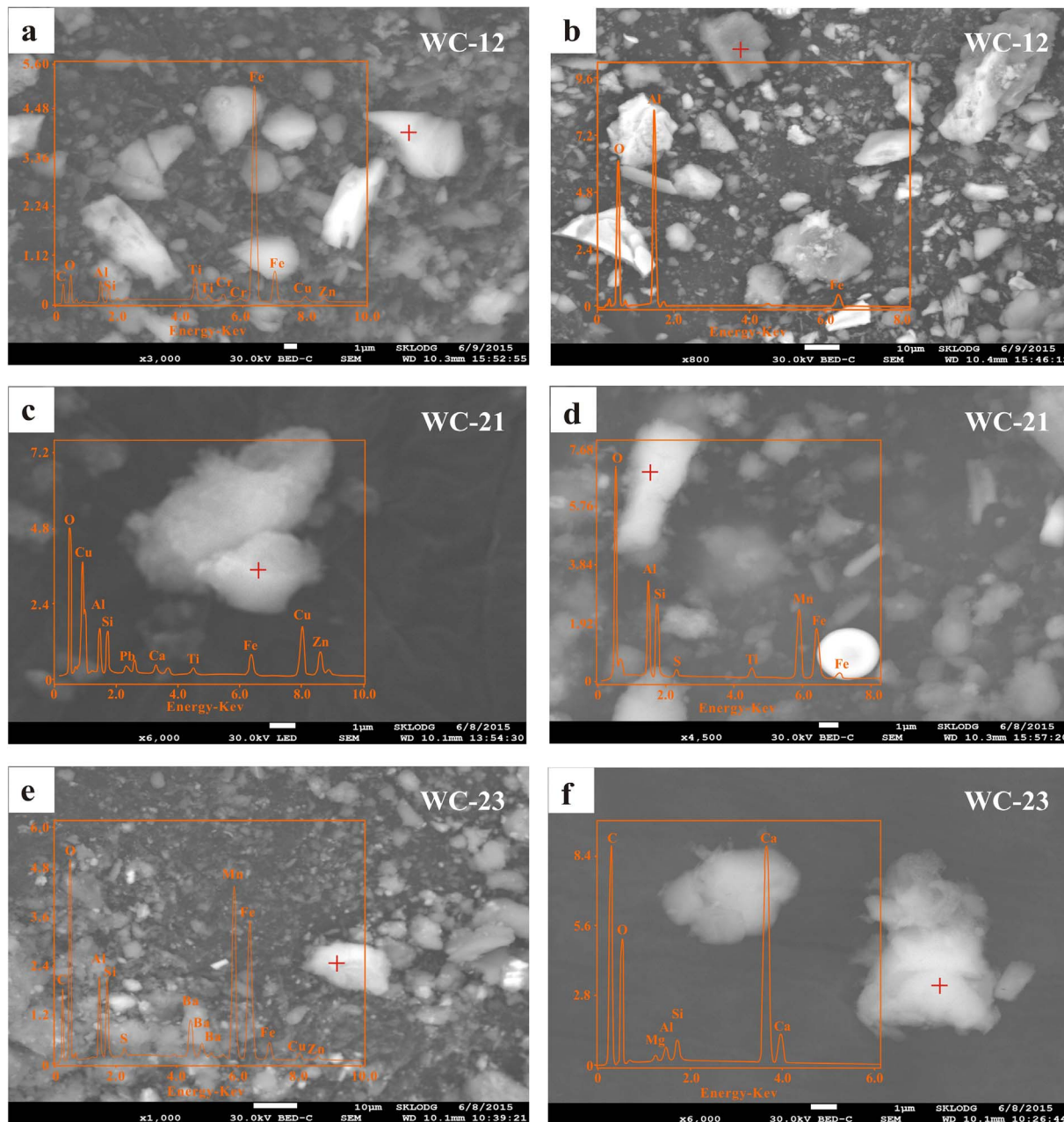


Fig. 3. SEM microphotographs and EDS spectra of representative grains (red cross) in the soil and saprolite samples from the Wenchang weathering profile. (a) irregularly-shaped Fe-Ti oxides grain in WC-12; (b) gibbsite grains in WC-12; (c) Cu-Zn enriched Fe oxides grains in WC-21; (d) Mn-(hydro)oxides grains in WC-21; (e) Ba-enriched Mn-(hydro)oxides grains in WC-23; and (f) irregular massive aggregates of carbonate mineral grains in WC-23. (g) columnar shaped Fe-Ti oxides grain in WC-28; (h) Ce-bearing oxides grains in WC-28; (i) Ce-bearing oxides grains in WC-36; (j) columnar shaped REE-bearing secondary phosphate grains in WC-51; (k) needle shaped REE-bearing secondary phosphate grains in WC-52; and (l) Ni-rich phosphate mineral grains in WC-52. (For interpretation of the references to color in this figure legend, the reader is referred to the web version of this article.)
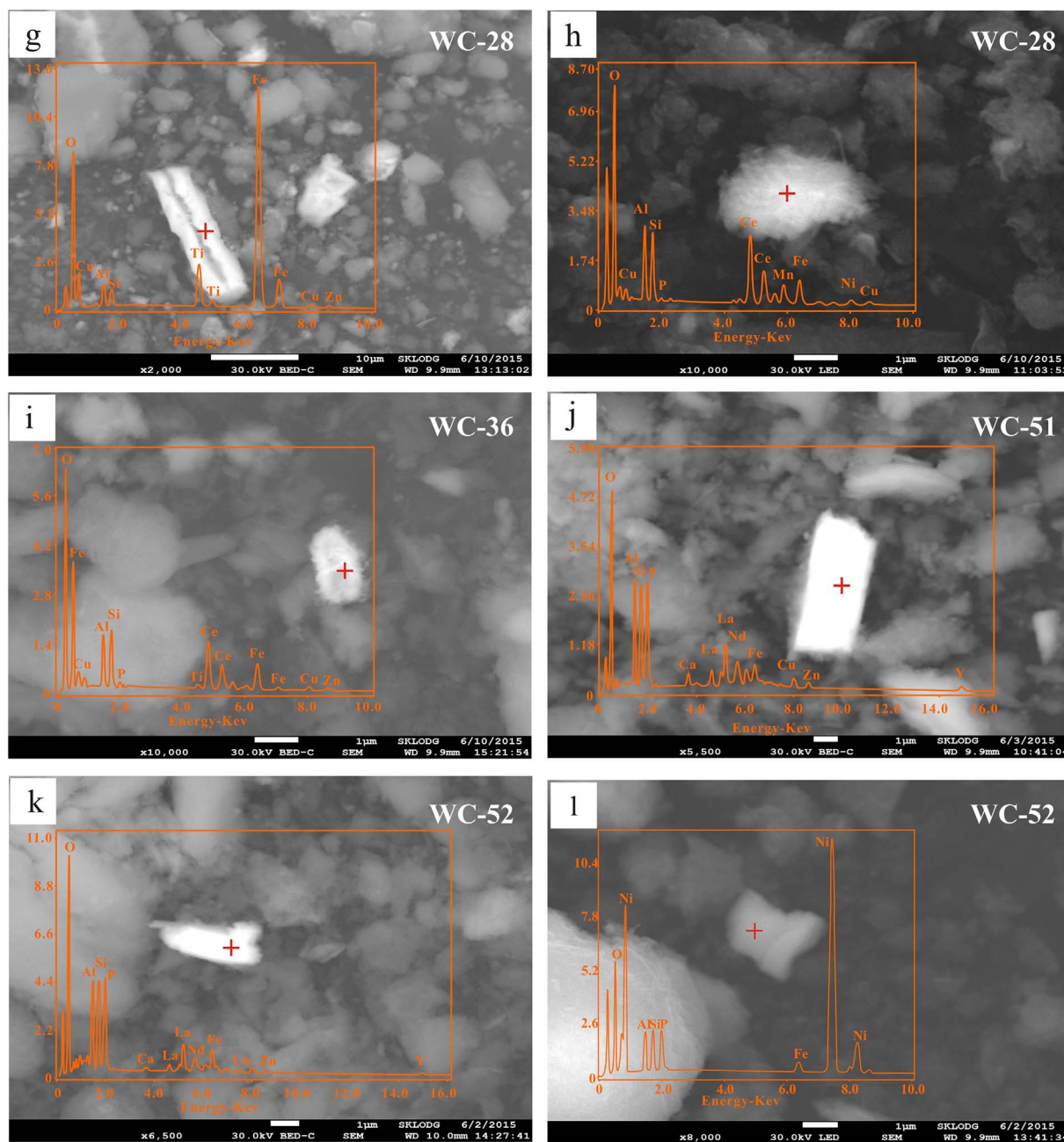
**Fig. 3.** (*continued*)

are coupled during extreme weathering of basalt. However, such coupling phenomena are not found in this study. On the contrary, our results (Fig. 5) reveal more complex variation trends of these elements. For example, for immobile elements (e.g., Al, Fe, Zr, Hf, Nb, Ta and Ti), oscillatory depletion and enrichment trend in $\tau_{Nb,j}$-depth profiles of these elements were found, while Mn and Co only show distinct enrichment at 6.1 m deep, and U and Ce mainly exhibit two to three enrichment peaks in the middle part of the saprolite. Phosphorus and Cr are generally depleted across the profile, but discernible enrichments (compared to those of surrounding samples) occur at the soil-saprolite and/or rock-regolith interfaces. Moreover, most alkali and alkaline earth metals (e.g., Rb, Sr, Cs, and Li) are strongly depleted across the profile, yet Ba and Be show enrichments at 6.1 m deep and/or at the rock-regolith interface, respectively. Transition metals (e.g. Cu, Zn, Ni, and Sc) exhibit marked enrichment peaks/net-gain at the soil-saprolite interface, the middle part (at 6.1 m deep), and rock-regolith interface of the profile (Fig. 5).

## 5. Discussion

### 5.1. Mineralogical and geochemical zonation of the Wenchang basalt weathering profile

Almost all elements in the soil horizon are leached, and these leached elements are reconcentrated in the middle-lower parts of the profile and along the rock-regolith interface. The depletion-enrichment profiles of these elements document the conversion of mineral phases and coupled dissolution and precipitation over time. One mineral dissolves to lose element $j$, whereas the other precipitates at a lower level to enrich element $j$ (Brantley and Lebedeva, 2011). Moreover, the oscillatory depletion and enrichment trends in $\tau_{Nb,j}$-depth profiles of immobile elements (e.g., Al, Fe, Zr, Hf, Ta and Ti) may reflect that such dissolution and precipitation processes are not equilibrium (Fig. 6). This study also identifies two discontinuities (soil-saprolite and rock-regolith interfaces) in terms of color, clay mineralogy and major/trace
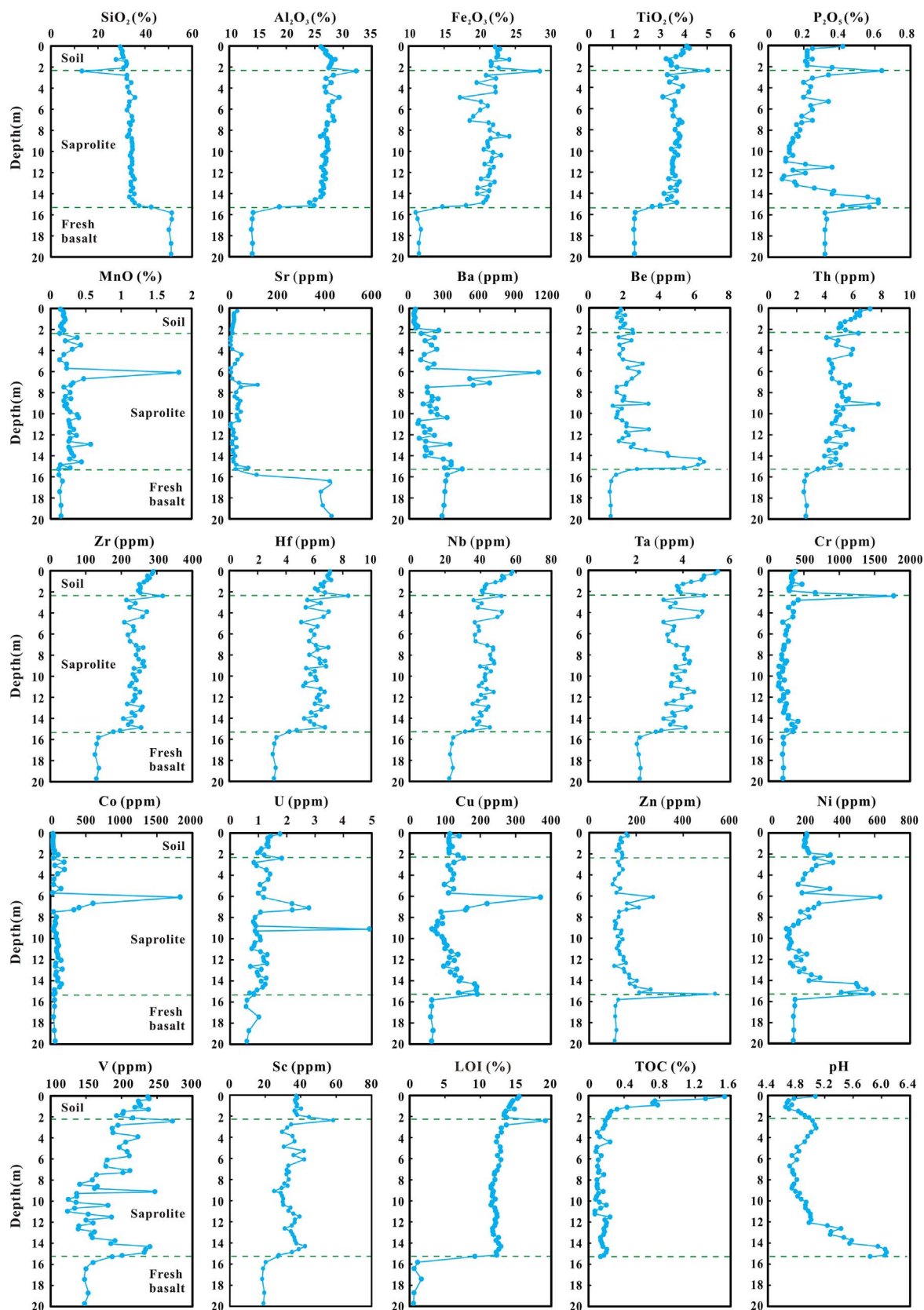
**Fig. 4.** Major and trace element concentrations, TOC contents and pH values across the Wenchang basalt weathering profile.

element compositions at 2.4 m and 15.28 m depth of the weathering profile (Fig. 6).

The soil-saprolite interface is marked by the maximum enrichments of $Al_2O_3$, $Fe_2O_3$, $TiO_2$, LOI and Cr, slight enrichments of immobile elements (Zr, Hf, Nb and Ta) and P, and depletion of $SiO_2$. The interface is also marked by the dominance of gibbsite and Fe-oxides/hydroxides and the color change from dark brick-red to light brick-red. The maximum LOI value, Al enrichment and gibbsite content near soil-saprolite
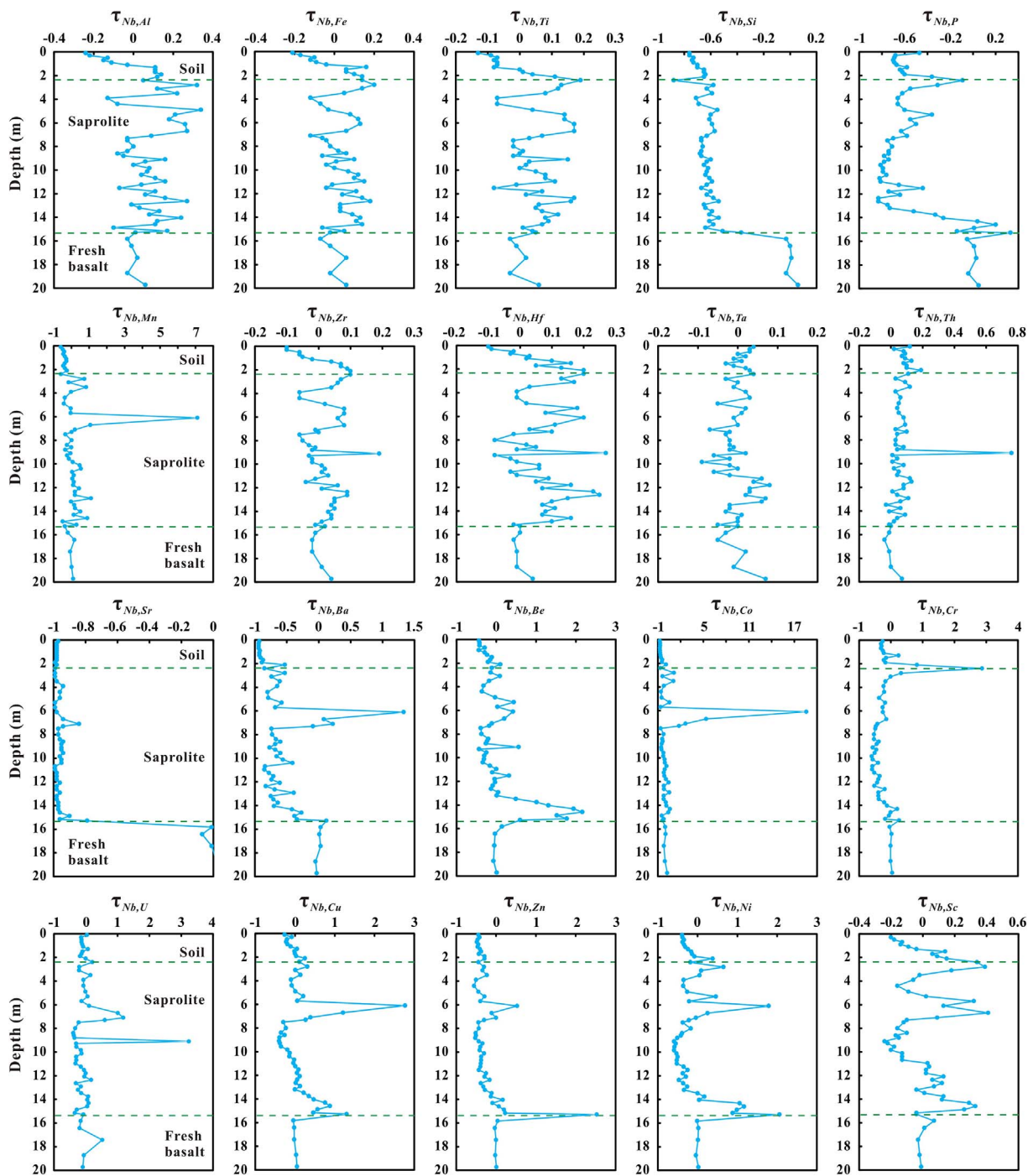
**Fig. 5.** Mass transfer coefficients ($\tau_{Nb,j}$) for major and trace elements across the Wenchang weathering profile.

interface, which was once interpreted to reflect the groundwater influence (Ma et al., 2007), may also indicate the maximum hydrolysis of kaolinite and gibbsite. This alternative interpretation is supported by: (1) the weathering profile is distinctly above the current regional water table (Fig. 1b); (2) the depth of the soil-saprolite interface is consistently (only varies slightly with the topography) (Fig. 1c); and (3) kaolinite dissolution and gibbsite formation were also found in the uppermost part (< 3 m deep) of the granite weathering profile developed under subtropical climate (Liu et al., 2016).

Above this discontinuity, macronutrients for plants such as P, Mg, Ca, Na, and K are strongly leached and depleted in the soil samples. The relative high concentrations of these elements and TOC in the uppermost sample (i.e., WC-1), compared to the other soil samples, may

indicate that they are derived from biogenetic source or contains possible anthropogenic fertilization (from pepper plantation) to the profile over time. The unidirectional attenuation of TOC content with increasing depth also indicates organic matter addition and decomposition during weathering and pedogenesis. The $\tau_{Nb,P}$ values of the soil samples at about 1 m are distinctly lower than those of the top and the bottom soil samples, indicating possible biogenetic pumping or uptake by root of vegetation. Therefore, we tend to interpret the maximum $P_2O_5$ concentration (0.64%) but slight depletion of P ($\tau_{Nb,P} = -0.09$) at the soil-saprolite interface as possible deposition of extraneous source P in the form of secondary phosphates.

Below this discontinuity, secondary carbonates precipitation (suggested by slight Sr enrichment) occurred at 3.9 and 7.1 m deep (see
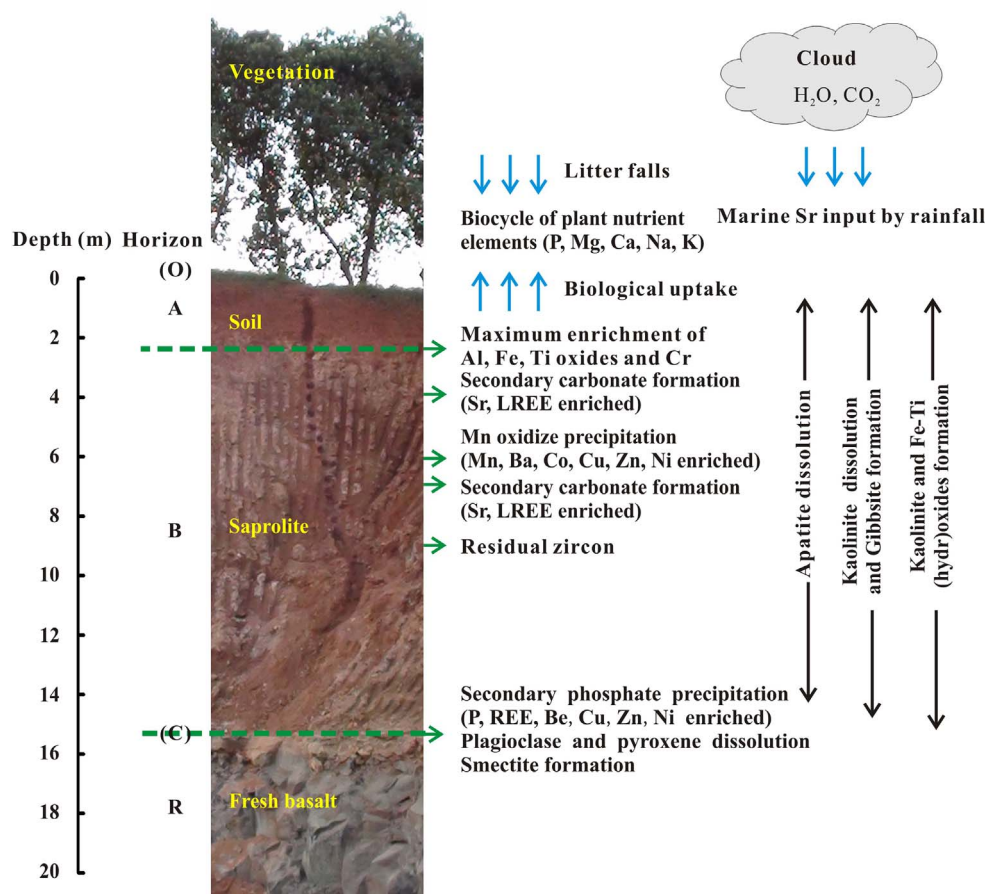
**Fig. 6.** Summarized geochemical model and zonations of major and trace elements along depth of the Wenchang basalt weathering profile.

discussion below). Secondary Mn oxide/hydroxide precipitated with enrichments of Co, Ba, Cu, Zn, Ni, and Sc at ~6.1 m deep. The presence of tiny secondary carbonate, quartz and even gypsum in the middle part of profile suggests relatively weak hydrodynamic or unsaturated soil solution conditions. These secondary minerals may have formed during the transition between dry and wet seasons. Sample WC-30 at 9.1 m deep exhibits distinct or slight enrichments of Th ($\tau_{Nb,Th}$ = 0.76), U ($\tau_{Nb,U}$ = 3.21), Hf ($\tau_{Nb,Hf}$ = 0.27) and Zr ($\tau_{Nb,Zr}$ = 0.19), indicating possible existence of residual zircon.

The rock-regolith interface is marked by the presence of yellowish semi-weathered basalt, secondary phosphate precipitation, and distinct enrichments of Be, Cu, Zn, Ni, Sc and V. The change of mineral and geochemical compositions between the basalt and its semi-weathered product illustrate the dissolution of primary mineral and formation of secondary mineral phases during the initial stage of weathering. Volcanic glass, plagioclase and augite are weathered at grossly similar rates during basalt or basaltic andesite weathering (Nesbitt and Wilson, 1992; Sak et al., 2010). The dissolution of glass, plagioclase, and pyroxene can be documented by the loss of K, Na, and Mg, respectively (Sak et al., 2010). Plagioclase and pyroxene, the two major mineral phases in the basalt, are only found in the semi-weathered basalt as indicated by XRD analyses. The limited thickness (15 cm) of the semi-weathered basalt horizon indicates that plagioclase and pyroxene are readily decomposed in the early weathering stage under tropical climate. Kaolinite, smectite and gibbsite are derived from the alteration of plagioclase and pyroxene, while Fe-oxides are mainly originated from the pyroxene alteration (Sak et al., 2010). Gibbsite can also be derived from the hydrolysis of kaolinite. Smectite formed during the early weathering stage may have been readily converted into kaolinite above the rock-regolith discontinuity. The distinct P enrichment in saprolite

and semi-weathered basalt samples near the rock-regolith interface represents the dissolution of primary apatite and the formation of secondary phosphate.

### 5.2. Mobilization and redistribution of alkali and alkaline earth metals

The concentrations of alkali and alkaline earth metals (e.g., Rb, Sr, Cs, Ba and Be) in the soil and saprolite samples are distinctly lower than those in the fresh basalt. The $\tau_{Nb,j}$ values of these elements are mostly negative, especially those for Rb and Sr are approaching -1, which indicate that most alkali and alkaline earth metals in basalt were strongly leached and transported out of the profile by soil solutions after extreme weathering.

For the soil samples, Sr concentration only shows distinct positive correlation with TOC content (R = 0.88, p < 0.001), which might suggest possible substitution of Sr for Ca, a macro-nutrient that is recycled by biological uptake and litter falls (Poszwa et al., 2000). Furthermore, Sr isotope evidences indicate that the addition of marine Sr would influence the Sr storage in the uppermost part of the basalt weathering profile of Hainan Island (Ma et al., 2010). For saprolite samples, however, there are no obvious correlations between Sr concentration and those of Al, Fe, Mn, P and TOC. In surficial environment, the stable form of Sr occurs mainly in carbonates (Mucci and Morse, 1983; Jin et al., 2006), and thus the mild Sr enrichment at 3.9 m and 7.1 m deep may be attributed to secondary carbonate precipitation.

Compared to other alkali and alkaline earth metals, Be exhibits lower net-loss in the soil and saprolite, and net-gain/enrichment occurs near the rock-regolith interface ($\tau_{Nb,Be}$ = 2.03). The Be concentrations in the soil and saprolite samples only show positive correlations with P content (Fig. 7a), and show subtle or negative correlations with Al, Fe,
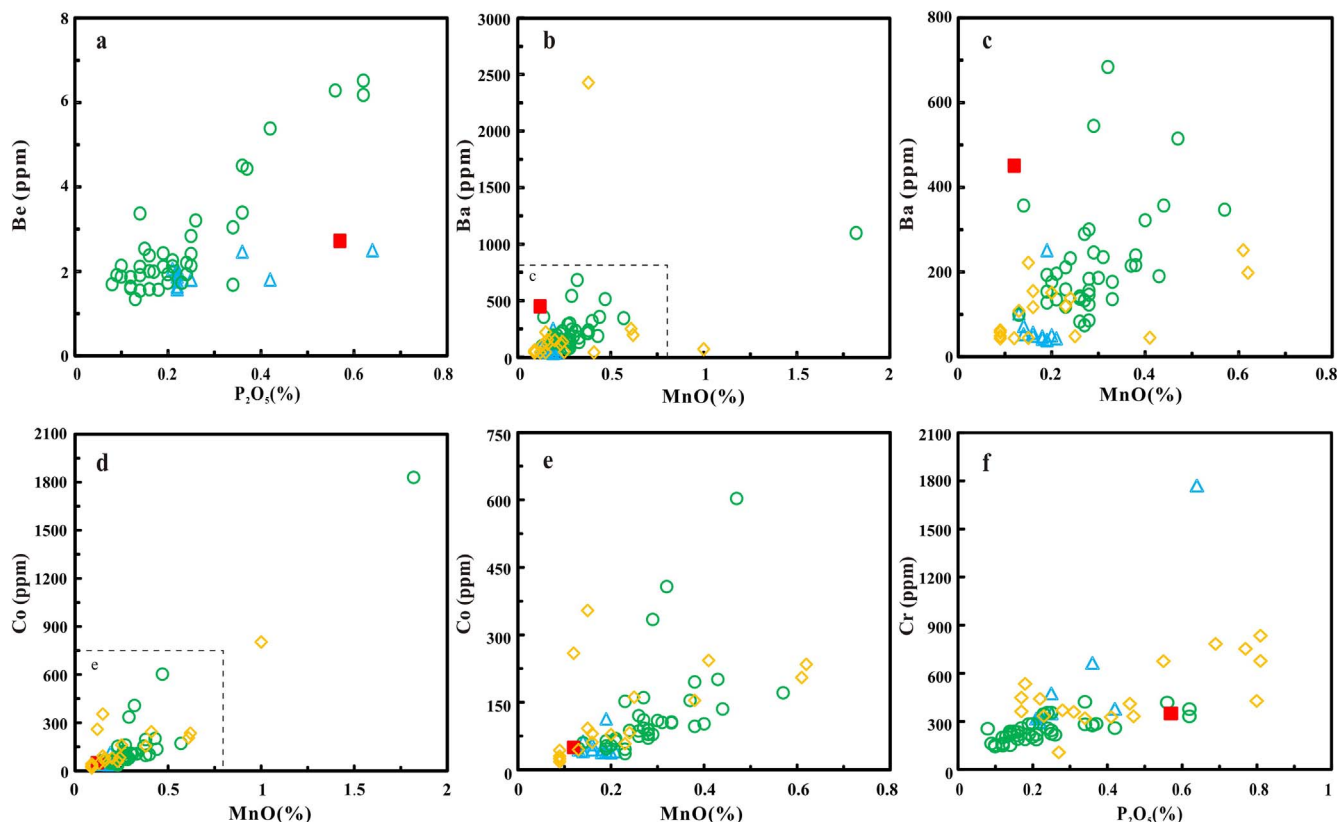
**Fig. 7.** Binary plots of (a) $P_2O_5$ vs. Be; (b) MnO vs. Ba; (c) MnO vs. Ba (for the samples with $MnO_2 < 0.70\%$); (d) MnO vs. Co; (e) MnO vs. Co (for the samples with $MnO_2 < 0.70\%$); and (f) $P_2O_5$ vs. Cr. The blue triangle, green circle, red square and orange diamond denote the soil, saprolite, semi-weathered basalt samples of this study and the saprolite samples from Ma et al. (2007), respectively. (For interpretation of the references to color in this figure legend, the reader is referred to the web version of this article.)

Mn and TOC contents. Therefore, elemental behavior of Be in basalt weathering profile is likely to be only affected by secondary phosphates, and the Be enrichment near the rock-regolith contact may have been related to the secondary phosphates accumulation there.

Barium is special in that the $\tau_{Nb,Ba}$ values of the soil and saprolite samples are mostly negative, but enrichment peak occurs at 6.1 m deep (maximum $\tau_{Nb,Ba} = 1.16$). Barium concentration in the soil and saprolite samples is positively correlated with MnO content (Fig. 7b and c), but does not show clear correlations with Al, Fe, P and TOC contents, especially for the saprolite samples. The maximum enrichment of Ba also coincides with that of Mn, and the SEM-EDS results demonstrate that the Mn-rich mineral grains contain some Ba. This suggests that under extreme weathering of basalts, the behavior of Ba may have been controlled by secondary Mn-oxides/hydroxides, and the enrichment of Ba at 6.1 m deep may have been associated with the secondary Mn-oxides/hydroxides accumulation there.

### 5.3. Mobilization and redistribution of redox-sensitive elements

Behaviors of varied valence elements, e.g., Mn, Co, Cr and U, are generally considered to be more sensitive to redox changes in chemical weathering processes (Guthrie and Kleeman, 1986; Middelburg et al., 1988; Collins and Kinsela, 2010; Kraemer et al., 2015; Zhang et al., 2015). In nature, cobalt occurs mainly as $Co^{2+}$ in solutions, whereas solubility of $Co^{3+}$ is very low (Collins and Kinsela, 2010). Similarly, $Mn^{2+}$ is more mobile than $Mn^{3+}$ (or $Mn^{4+}$), which would be precipitated as insoluble Mn-oxides/hydroxides (Van der Weijden and Van der Weijden, 1995; Koppi et al., 1996). On the contrary, U and Cr ions exhibit opposite dissolving behaviors at different valence. The more

reduced $Cr^{3+}$ state is insoluble and immobile (Ellis et al., 2002), and under oxidation states Cr mainly forms soluble, oxygen-bearing anions, and transport as chromate or dichromate (Ellis et al., 2002; Oze et al., 2007; Berger and Frei, 2014). Uranium is generally more mobile in oxidized environment, in which $U^{4+}$ is oxidized into the more stable $U^{6+}$ (in the form of uranyl ion ($UO_2^{2+}$)) in solutions (Duff et al., 2002). In contrast, the reduced form ($U^{4+}$) would precipitate and concentrated as $UO_2$, $U_3O_8$ or surface active carboxyl complexes (Klinkhammer and Palmer, 1991). Therefore, depending on the differences of redox potentials of these ions (Fig. 8) and redox condition of the weathering profile, these elements can be enriched at different depths.

The surficial ($< 45$ cm) laterite in the Hainan basalt exhibits relatively high Eh values (0.63–0.72 V; Ding, 2008). The yellowish saprolite and semi-weathered basalt near the regolith-rock interface indicates increasing content of goethite (or $Fe^{2+}$) in these samples (Torrent et al., 1983) or the Fe redox condition at this depth has changed from being oxidized to reduced. Using the pH-Eh diagram (Fig. 8a) and measured pH values ($\sim 6$) of these sample, the upper limit of Eh values ($\sim 0.2$ V) can be approximately estimated. Ma et al. (2007) suggested an oxic environment in the middle part of the profile, and a reduced environment in the upper part of the profile, based on the vertical variations of TOC and total nitrogen along depth. However, the unidirectional attenuation of TOC content along the depth of this profile (Fig. 4) and high Eh values of surficial ($< 45$ cm) laterite in Hainan (Ding, 2008) do not support such conclusion.

In the measured pH (4.65–6.07) or considered Eh ($\sim 0.2$–0.72 V) conditions, Mn can occur in two different forms, i.e., $Mn^{2+}$ and $MnO_2$ (Fig. 8a). Therefore, the Mn enrichment at 6.1 m deep may have been led by the oxidation of soluble $Mn^{2+}$ into insoluble $Mn^{3+}$ (or $Mn^{4+}$) or
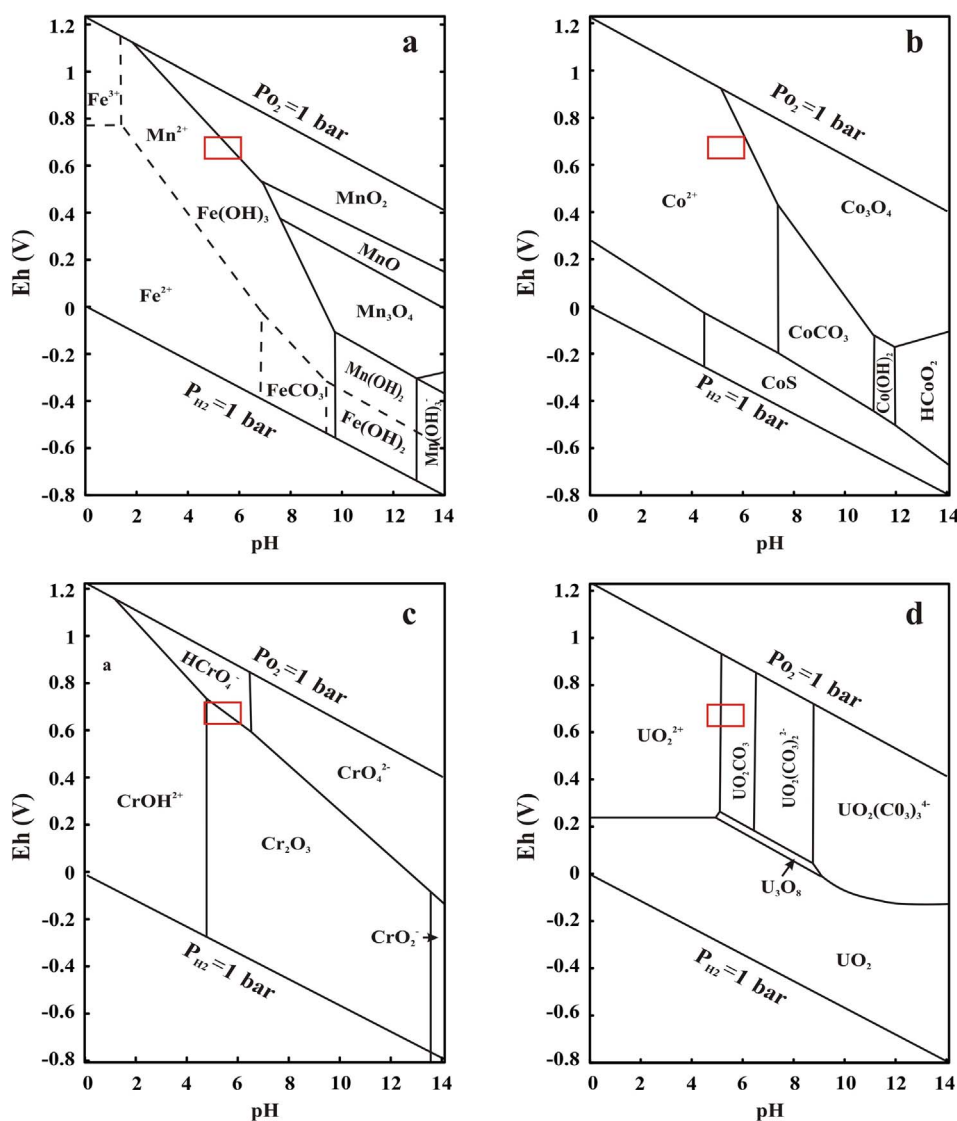
**Fig. 8.** pH-Eh diagrams for the elements: (a) Mn and Fe (dash line); (b) Co; (c) Cr and (d) U. Assumed activity of Fe, Mn, Co, Cr and U are $10^{-6}$ M, $10^{-6}$ M, $10^{-6}$ M, $10^{-6}$ M and $10^{-6, -8}$ M, respectively (data from Brookins, 1988). Red box indicates the Eh and pH ranges of the soil and saprolite samples. The pH values are from this study, while the Eh values are from the surficial (< 45 cm) laterite samples from the primitive rain forest in Jianfengling, Hainan Island (Ding, 2008). (For interpretation of the references to color in this figure legend, the reader is referred to the web version of this article.)

by dissolution of $Mn^{2+}$-bearing oxides during progressing weathering. The latter interpretation can avoid the awkwardness of migration of insoluble $Mn^{3+}$ in oxidized soil and oxidation of soluble $Mn^{2+}$ in possible reduced saprolites. Although Co can also be oxidized into the insoluble $Co^{3+}$, Co mainly occurs in a soluble $Co^{2+}$ state in the Eh-pH conditions of this study (Fig. 8b). The generally positive correlation between Co and Mn concentrations (Fig. 7d and e), and the coincidence of their net-gain ($\tau_{Nb,Mn}$ = 7.11; $\tau_{Nb,Co}$ = 18.59) at near 6.1 m, demonstrate that the Co enrichment may have been influenced by the adsorption of secondary Mn-oxides/hydroxides (Bradl, 2004; Ling et al., 2015).

The Cr enrichment in weathering profiles has been attributed to the Cr adsorption on secondary Fe-oxides/hydroxides (Topp et al., 1984) or on organic matters (Dupré et al., 1999; O'Connor et al., 2015). Nevertheless, we notice that in the Wenchang basalt weathering profile: (1) Distinct Cr enrichment only occurs near the soil-saprolite interface, and the samples from there also contain relatively high $Al_2O_3$ and $Fe_2O_3$ contents; (2) Both the soil and saprolite samples exhibit generally

positive Cr vs. $P_2O_5$ correlation (Fig. 7f), whereas the correlations of Cr with Al, Fe, Mn and TOC contents are unclear; (3) Under the pH-Eh condition of the Hainan latosols, Cr occurs mainly as $Cr^{6+}$ ions (Fig. 8c). This indicates that the migration of $Cr^{6+}$ under oxidized condition is limited and Cr is mainly adsorbed on secondary phosphates during extreme weathering of basalts.

Both Fe (II)-bearing minerals and the $Fe^{2+}$ that absorbs on Fe (III) minerals can act as reductants for $U^{6+}$ (Fredrickson et al., 2000; Behrends and Van Cappellen, 2005), and the uranyl ions can also be absorbed onto secondary Fe-oxides/hydroxides or clay mineral surface (Van der Weijden and Van der Weijden, 1995; Boekhout et al., 2015). Besides, uranium precipitation and enrichment in the soil may also be associated with the activities of dissolved phosphates and carbonates in the soil solution (Jerden et al., 2003; Duff et al., 2002; Boekhout et al., 2015), and the amalgamation between $U^{6+}$ and secondary phosphates may also lead to U concentration in the soil profile (Jerden et al., 2003). Nevertheless, correlations between U concentration and Al, Fe, Mn, P and TOC contents are not obvious for most of the samples. Under pH-Eh
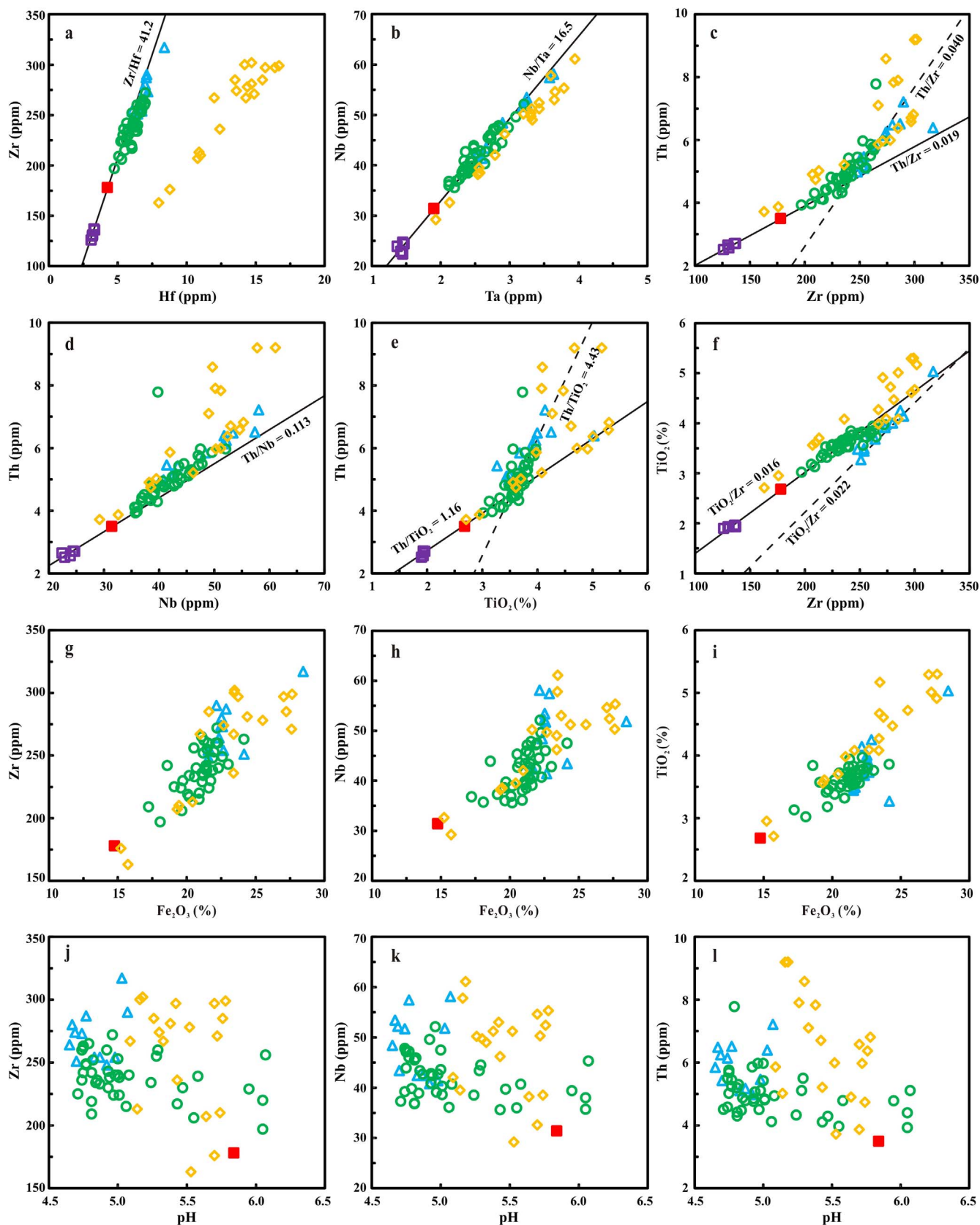
**Fig. 9.** Binary plots of (a) Zr vs. Hf; (b) Nb vs. Ta; (c) Th vs. Zr; (d) Th vs. Nb; (e) Th vs. TiO$_2$; (f) TiO$_2$ vs. Zr; (g) Zr vs. Fe$_2$O$_3$; (h) Nb vs. Fe$_2$O$_3$; (i) TiO$_2$ vs. Fe$_2$O$_3$; (j) Zr vs. pH; (k) Nb vs. pH; and (l) Th vs pH. The blue triangle, green circle, red solid square, purple open square and orange diamond denote the soil, saprolite, semi-weathered basalt, fresh basalt samples of this study and saprolite samples from Ma et al. (2007), respectively. (For interpretation of the references to color in this figure legend, the reader is referred to the web version of this article.)
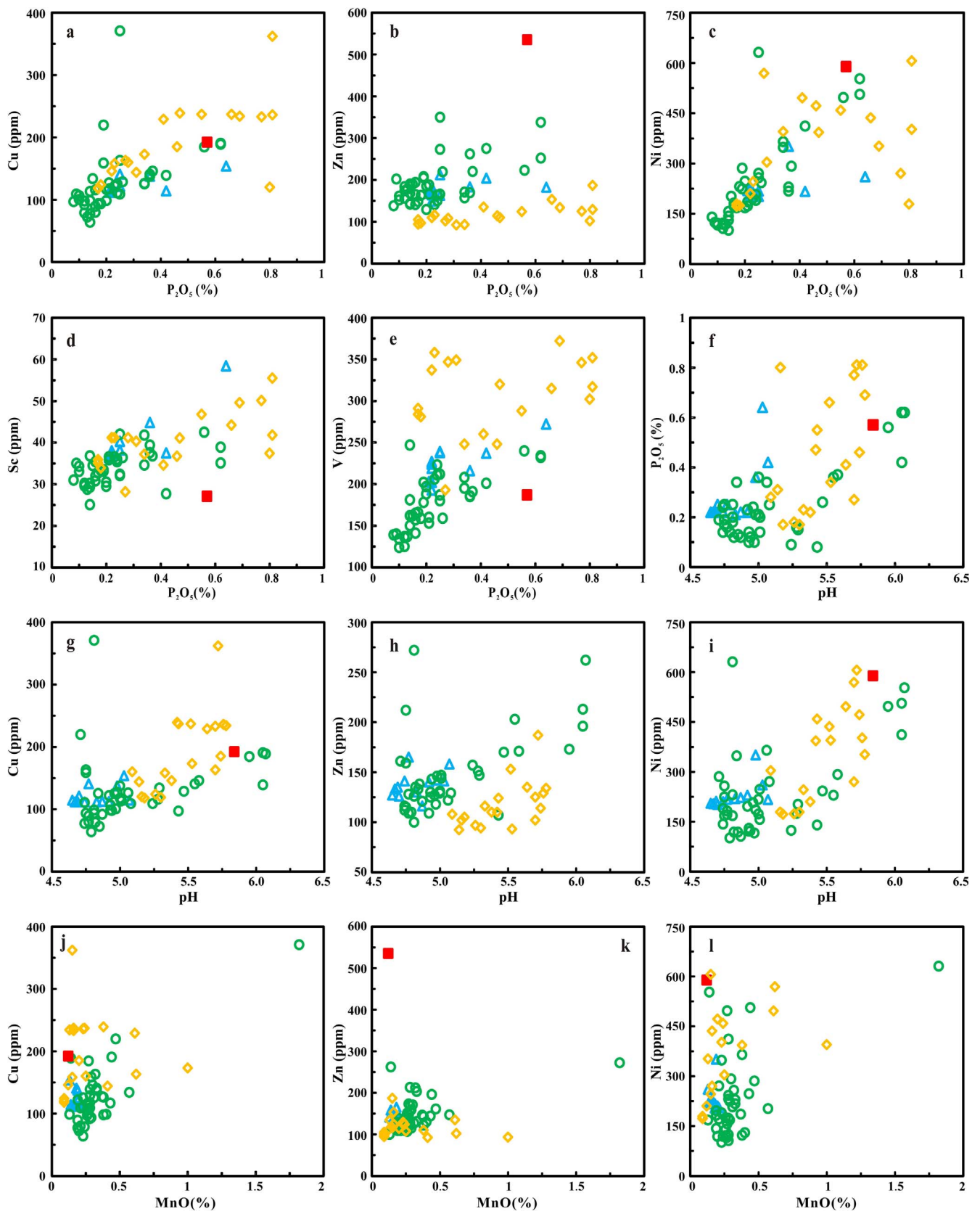
**Fig. 10.** Binary plots of P$_2$O$_5$ vs. Cu (a); Zn (b); Ni (c); Sc (d) and V (e); pH vs. P$_2$O$_5$ (f); Cu (g); Zn (h) and Ni (i); and MnO vs. Cu (j); Zn (k); Ni (l). The blue triangles, green circles, red full squares and orange diamonds denote the soil, saprolite, semi-weathered basalt samples of this study and saprolite samples from Ma et al. (2007), respectively. (For interpretation of the references to color in this figure legend, the reader is referred to the web version of this article.)

conditions of the profile studied and even more reduced but similar pH conditions, uranium occurs mainly as $U^{6+}$ ($UO_2^{2+}$ and $UO_2CO_3$) (Fig. 8d). Therefore, the mild U enrichment in the middle part of the profile ($\sim$7.1 m deep) is very likely to be caused by the decomposition of uranyl carbonate ions or the reduction and precipitation of $U^{6+}$ into the insoluble $U^{4+}$.

### 5.4. Mobilization and redistribution of immobile elements

#### 5.4.1. Nb/Ta and Zr/Hf ratios

The Zr/Hf and Nb/Ta ratios of the soil and saprolite samples range from 35.9 to 43.5 (average: 39.4, n = 52) and 15.3 to 18.0 (average 16.5, n = 52), respectively. These Zr/Hf ratios are distinctly higher than those (17.9–23.7) based on the reported Zr and Hf concentrations for saprolite (Ma et al., 2007), and such lower Zr/Hf ratios may be caused by overestimated Hf concentrations. For example, Hf concentrations (5.02–5.36 ppm) of basalts reported by Ma et al. (2007) are about 1.6 times higher than those of our results (3.07–3.33 ppm, 3.21 ppm on average, n = 5). Our average values are consistent with those of the northern Hainan basalts (Zr/Hf = 36.6, Nb/Ta = 16.1; Liu et al., 2015) and the basalt standard (BHVO-1) (Zr/Hf = 39.3, Nb/Ta = 16.0; Babechuk et al., 2015). In the Zr vs. Hf and Nb vs. Ta scatter diagrams (Fig. 9a and b), the soil and saprolite samples from the Wenchang basalt weathering profile are generally distributed along the basalt weathering trend line (BWTL, illustrated by the solid lines in Fig. 10a–f), which is defined by the average composition of basalts and semi-weathered basalt. Because the Zr/Hf and Nb/Ta ratios would not change significantly during weathering (Young and Nesbitt, 1998; Kurtz et al., 2000; Du et al., 2012; Babechuk et al., 2015), we deduced that the mobility of these isovalent geochemical twins (Zr-Hf and Nb-Ta) are similar during weathering, and the profile studied is formed by in-situ extreme weathering of basalt.

#### 5.4.2. Different mobility of Th, Zr, Nb and Ti

Babechuk et al. (2014, 2015) noticed that when the ratios of the high field strength elements (HFSE) or immobile elements with different valence and ionic radii (e.g., Hf/Ta, Zr/Nb, Th/Nb and Al/Ti) are concern, a discrete ratio offset is evident between those ratios of basaltic lava flows and weathered saprolite, and they tend to explain such offset or excursion by the addition of aeolian deposition during chemical weathering. For the Wenchang weathering profile, the offsets of Th/Zr, Th/Ti and Ti/Zr ratios between basalts, semi-weathered basalt, saprolite and soil samples become more obvious with increasing of Th, Zr and Ti concentrations. Especially, in the Th vs. Zr, Th vs. Ti and Zr vs. Ti diagrams (Fig. 9c, e and f), the soil and saprolite samples with Th (> 4.5 ppm), TiO$_2$ (> 3.50%), and Zr (> 230 ppm) are distinctly deviated from the BWTL, and these samples from the upper part of the profile exhibit increasing Th/Zr, Th/Ti and Ti/Zr ratios (illustrated by the dashed lines in Fig. 9c, e and f). These offsets are fully coincided with the results of mass balance calculations. For example, when Th was selected as the reference element, Zr and Ti are depleted, and when Zr and Ti were selected as the reference elements, Th is enriched (see the Appendix B).

With the exception of one sample (WC-30) for possible residence of zircon, the average Th/Nb ratios of soil, saprolite, semi-weathered basalt, and basalt samples from the Wenchang weathering profile are 0.122, 0.119, 0.112, and 0.111, respectively. Most soil and saprolite samples are distributed along the BWTL in Th vs. Nb diagram (Fig. 9d). On the contrary, the loess derived from the Loess Plateau in North China exhibits higher Th/Nb (Th/Nb = 0.89) and Zr/Nb (Zr/Nb = 14.6) ratios, and lower Nb/Ta ratios (8.40) (Jahn et al., 2001). If the increasing Th/Zr, Th/Ti and Ti/Zr ratios of the soil and saprolite samples from the upper part of the profile were caused by loess

deposition, increasing Th/Nb and Zr/Nb ratios and decreasing Nb/Ta ratios should be found in these samples. However, the nearly constant Th/Nb and Nb/Ta ratios of most soil and saprolite samples do not support such explanation. More importantly, Nd-Hf isotope evidence of saprolite samples from regional basalt weathering profile indicates the contributions of extraneous Nd and Hf both from wet and dry deposits of aeolian input are negligible (Ma et al., 2010).

The increasing Th/Zr, Th/Ti and Ti/Zr ratios of the soil and saprolite samples from the upper part of the profile may be mainly controlled by the weathering susceptibility of primary minerals containing these elements and the stability of hydrated ions of these elements during chemical weathering processes (Du et al., 2012). The main Zr-bearing accessory minerals in igneous rocks, such as zircon, are also corroded and partially dissolved in extremely weathered lateritic environment (Braun et al., 1993; Du et al., 2012). Titanium has been known to become mobile when ilmenite alters to secondary rutile and anatase, and can occur as a dissolved form under tropical weathering condition (Cornu et al., 1999; Du et al., 2012). Moreover, Ti fractionates from Zr during extreme weathering and advanced lateritization (Hill et al., 2000; Du et al., 2012). Kurtz et al. (2000) found that Zr, Hf, Al are depleted relative to Nb in surface soil horizons but are enriched at depth. Therefore, the increasing Th/Zr, Th/Ti and Ti/Zr ratios of soil and saprolite samples from the upper part of the Wenchang weathering profile can be attributed to significant depletion and fractionation of Zr and Ti, instead of the addition of Th. Therefore, a stability sequence for immobile elements can be summarized as Nb $\approx$ Ta $\approx$ Th > Zr $\approx$ Hf > Ti during extreme weathering process of the Wenchang basalt weathering profile.

#### 5.4.3. Iron concentration, pH and mobilization of immobile element

Additionally, for most of the soil and saprolite samples, the Zr, Nb and Ti concentrations are positively correlated with Fe contents (Fig. 9g–i), whereas the correlations of Fe with Al, Mn, P and TOC contents are not obvious. Moreover, the variation trends of concentrations and $\tau_{Nb,j}$ values (with depths) of immobile elements (e.g., Zr, Hf, Nb and Ta) are highly similar to those of Fe. Therefore, the immobile elemental behaviors may be mainly controlled by the formation of secondary Fe oxides/hydroxides during basalt extreme weathering. Moreover, immobile element concentrations in the soil and saprolite samples show weak negative correlation with the soil pH values (Fig. 9j–l), indicating that the fluctuant enrichment or depletion of these elements in the soil and saprolite samples may also be affected by the pH changes.

Leaching and enrichment of immobile elements in the soil horizon may be related to the following factors: (1) Under acidic condition, extensive leaching of mobile elements may occur; (2) Organic acid, dissolved organic matters and microbial activities in the soil may facilitate the decomposition of resistate minerals (Tejian-Kella et al., 1991; Ehrlich, 1998; Dontsova et al., 2014); and (3) Organic matters (and the colloidal matters formed after their decomposition) of the soil may also facilitate the transportation of immobile elements (Viers et al., 2000; Oliva et al., 1999; Pokrovsky and Schott, 2002; Dupré et al., 1999; Kurtz et al., 2000; Braun et al., 2005; Pokrovsky et al., 2006; Brantley and Lebedeva, 2011; Kraemer et al., 2015).

### 5.5. Mobilization and redistribution of transition metals

For the transition metals, we noticed that: (1) Copper, Zn, Ni, Sc and V concentrations are positively correlated with P contents in most soil and saprolite samples (Fig. 10a–e); (2) Similar to P, the Cu, Zn and Ni concentrations show varying positive correlations with the pH values (Fig. 10f–i); (3) The samples with highest Mn contents also contain relatively high Cu and Ni concentrations. Nevertheless, the correlations

between Mn contents and other transition metals are not obvious (Fig. 10j–l); (4) The enrichments of transition metals and $P_2O_5$ coincide near the rock-regolith interface. In addition, SEM-EDS studies reveal secondary phosphate grains that contain some Ni (Fig. 3g). Moreover, Vircava et al. (2015) found that the transformation from aluminum phosphate - sulfate minerals to secondary apatite precipitates in a Neoproterozoic Baltic paleosol reflects changes in pH. All these suggest that elemental behaviors of transition metals are mainly controlled by secondary phosphates during extreme weathering of basalts.

*5.6. Implications on isotopic fractionation during extreme weathering of basalts*

Based on the same sample set collected from one basalt weathering profile, which was firstly studied by Ma et al. (2007) and is very close to our new profile, Mg, Cu and Fe isotopic systems and isotope fractionation during extreme weathering of basalt in Hainan Island have been measured and discussed (Huang et al., 2012; Liu et al., 2014). Although the phosphorus contents of saprolite samples in the lower section (bellow 3 m) are generally higher than those in the upper section (above 3 m) of this profile, the possible link between secondary phosphate and Mg, Cu isotope fractionation has never been discussed.

The adsorption and desorption processes of kaolin minerals were proposed to interpret the variations of Mg concentration ($< 2\%$) and isotopic compositions ($\delta^{26}$Mg values range from $-0.49‰$ to $0.40‰$) of saprolite samples from this profile (Huang et al., 2012). We noticed that $\delta^{26}$Mg are positively correlated with $\tau_{Nb, \, Mg}$ values of saprolite samples from this profile (Huang et al., 2012), which means that Mg isotopic composition are also governed by the factors controlling Mg concentration of saprolite samples. Our analytical data show distinct MgO vs. CaO correlation in the soil and saprolite samples (R = 0.896, p < 0.001, n = 51, except sample WC-1), and CaO occurs at least in two different forms, i.e., secondary carbonates and phosphates. Considering the similar geochemical behavior of Ca and Mg, $Mg^{2+}$ may enter insoluble secondary phosphate, which is supported by the positive correlation between Mg and Y (an element that only hosted in secondary phosphate as indentified by SEM-EDS analysis) (R = 0.95, p < 0.001, n = 51, expect sample WC-50).

The behavior of Cu isotopes during extreme weathering is similar to that of Mg isotopes. The positive $\delta^{65}$Cu vs. $\tau_{Th, \, Cu}$ correlation in the Hainan weathering profile indicates that heavy Cu isotopes ($^{65}$Cu) are leached out and the weathered residues are isotopically light (Liu et al., 2014). Furthermore, $\delta^{65}$Cu is negatively correlated with the TOC content throughout the profile, which has been interpreted as Cu isotope fractionation between organic ligand-bound Cu and dissolved (desorbed) Cu (with the former being isotopically lighter), and biological cycling plays an important role in governing the Cu isotopic variation across the profile depth (Liu et al., 2014). Moreover, Ni-bearing clay minerals and Fe-oxides can account for the Ni isotope fractionation during tropical weathering of ultramafic rocks (Ratié et al., 2015).

However, Cu (or $\tau_{Nb, \, Cu}$) vs. TOC correlations are absent in our soil and saprolite samples, which indicate that the concentrations and elemental behaviors of transition metals (e.g., Cu and Ni) are mainly controlled by the formation of secondary phosphates by extreme weathering of basalts.

## 6. Conclusions

The well-developed and complete basalt weathering profile ($> 15$ m thick) on the Hainan Island in South China is typical of basalt weathering and pedogenesis in tropical climate. The soil and saprolite samples from this profile are characterized by high $Al_2O_3$ and $Fe_2O_3$ concentrations (up to 32.3% and 28.5%, respectively), as well as kaolinite, Fe-oxides/hydroxides and gibbsite (or boehmite) dominated mineral assemblage. This indicates that the profile has undergone extensive desilicate and ferrallitic weathering under tropical climate. The acidic and organic-rich environment in the soil horizon may have promoted elemental remobilization and leaching. The strongest $SiO_2$ depletion, $Al_2O_3$ enrichment, kaolinite hydrolysis and gibbsite formation all occur near the soil-saprolite interface ($\sim 2.4$ m deep). The mild Sr reconcentration (at $\sim 3.9$ m and $\sim 7.1$ m deep) may be attributed to the precipitation of secondary carbonates. Manganese-oxides/hydroxides may have precipitated at 6.1 m deep, accompanied by the maximum enrichment of Ba and Co. Uranium is mildly enriched in the middle part (at $\sim 7.1$ m and $\sim 9.1$ m deep) and may be caused by the decomposition of uranyl carbonates or the presence of zircon. Elemental behaviors of the immobile Zr, Hf, Nb and Ta along depth are mainly controlled by the formation of secondary Fe-oxides/hydroxides, and follow the stability sequence of Nb $\approx$ Ta $\approx$ Th $>$ Zr $\approx$ Hf $>$ Ti. Plagioclase, pyroxene and apatite are quickly dissolved and converted to kaolinite, smectite, Fe-oxides and secondary phosphates along the rock-regolith interface in the early weathering stage. The marked enrichments of transition metals (such as Cu, Zn, Ni, and Sc), Be and Cr along the soil-saprolite and rock-regolith interfaces may have been mainly associated with the secondary phosphates and pH increase there, and the secondary phosphate formation may have redistributed some transition metals, and possibly also fractionated the Mg, Cu and Ni isotope systems.

## A. Soil particle size analyses and profile description

About 200 mg of each soil and saprolite sample (possible root traces were picked out) was treated with water, 10% HCl and 10% $H_2O_2$, respectively, to remove possible carbonates and organic matter. After drying, the samples were grounded to less than 200 μm, and then a laser size analyser (MALVERN, APA-2000, UK) was employed to analyze the particle size distributions of soil and saprolite samples at the State Key Laboratory of Environmental Geochemistry (IGCAS). The particle size distributions are categorized into three major parts: clay ($< 2$μm), silt (2–20 μm), and sand (20–200 μm), and the percentages of each part were quantified. Full analytical results and profile and sample descriptions were given in Table A1.

**Table A1**

The sample descriptions and particle size analyses results of the Wenchang weathering profile.

| Sample no. | Sample type | Depth (m) | Horizon | Color (dry) | | Soil structure | Biological activity | Clay (%) | Silt (%) | Sand (%) |
|---|---|---|---|---|---|---|---|---|---|---|
| WC-1 | Soil | 0.1 | A | 10R4/5 | Red | Clastic peds | Fine to medium root traces | 20.8 | 52.2 | 27.0 |
| WC-2 | Soil | 0.3 | A | 10R4/5 | Red | Clastic peds | Fine to medium root traces | 15.9 | 47.2 | 36.9 |
| WC-3 | Soil | 0.5 | A | 10R4/6 | Red | Clastic peds | Fine to medium root traces | 21.9 | 50.3 | 27.8 |
| WC-4 | Soil | 0.7 | A | 10R4/5 | Red | Clastic peds | Fine root traces | 13.7 | 41.4 | 44.9 |
| WC-5 | Soil | 0.9 | A | 10R4/6 | Red | Clastic peds | Fine root traces | 9.5 | 22.7 | 67.8 |
| WC-6 | Soil | 1.1 | A | 10R4/5 | Red | Clastic peds | Fine root traces | 10.2 | 33.8 | 55.9 |
| WC-7 | Soil | 1.3 | A | 10R4/6 | Red | Crumb peds | Rare fine root traces | 20.8 | 54.5 | 24.7 |
| WC-8 | Soil | 1.5 | A | 10R4/5 | Red | Crumb peds | Rare fine root traces | 18.1 | 52.2 | 29.7 |
| WC-9 | Soil | 1.7 | A | 10R4/6 | Red | Crumb peds | × | 11.7 | 32.2 | 56.2 |
| WC-10 | Soil | 1.9 | A | 10R4/5 | Red | Crumb peds | × | 16.0 | 50.6 | 33.4 |
| WC-11 | Soil | 2.1 | A | 5YR3/7 | Yellowish red | Crumb peds | × | 14.0 | 48.9 | 37.1 |
| WC-12 | Soil | 2.4 | A | 5YR6/7 | Reddish yellow | Crumb peds | × | 8.8 | 33.8 | 57.4 |
| WC-13 | Saprolite | 2.8 | B | 5YR3/6 | Yellowish red | Angular blocky peds | × | 5.6 | 29.8 | 64.7 |
| WC-14 | Saprolite | 3.1 | B | 10R4/5 | Red | Angular blocky peds | × | 6.7 | 24.3 | 68.9 |
| WC-15 | Saprolite | 3.5 | B | 10R4/6 | Red | Angular blocky peds | × | 7.9 | 24.0 | 68.1 |
| WC-16 | Saprolite | 3.9 | B | 5R5/3 | Weak red | Angular blocky peds | × | 10.7 | 43.5 | 45.7 |
| WC-17 | Saprolite | 4.4 | B | 5R4/3 | Weak red | Angular blocky peds | × | 7.5 | 25.0 | 67.5 |
| WC-18 | Saprolite | 4.9 | B | 5R5/3 | Weak red | Angular blocky peds | × | 6.8 | 21.4 | 71.8 |
| WC-19 | Saprolite | 5.3 | B | 2.5YR5/3 | Reddish brown | Angular blocky peds | × | 8.1 | 22.5 | 69.4 |
| WC-20 | Saprolite | 5.7 | B | 5R4/3 | Weak red | Angular blocky peds | × | 6.0 | 21.6 | 72.4 |
| WC-21 | Saprolite | 6.1 | B | 2.5YR5/3 | Reddish brown | Angular blocky peds | × | 12.1 | 48.1 | 39.8 |
| WC-22 | Saprolite | 6.7 | B | 2.5YR4/3 | Reddish brown | Angular blocky peds | × | 7.4 | 23.7 | 68.9 |
| WC-23 | Saprolite | 7.1 | B | 2.5YR4/4 | Reddish brown | Angular blocky peds | × | 6.9 | 21.5 | 71.6 |
| WC-24 | Saprolite | 7.3 | B | 2.5YR4/4 | Reddish brown | Angular blocky peds | × | 8.7 | 25.5 | 65.8 |
| WC-25 | Saprolite | 7.5 | B | 2.5YR4/3 | Reddish brown | Angular blocky peds | × | 12.3 | 44.5 | 43.1 |
| WC-26 | Saprolite | 8 | B | 2.5YR4/3 | Reddish brown | Angular blocky peds | × | 6.7 | 42.8 | 50.5 |
| WC-27 | Saprolite | 8.4 | B | 5R5/3 | Weak red | Angular blocky peds | × | 6.8 | 44.9 | 48.3 |
| WC-28 | Saprolite | 8.6 | B | 5R4/3 | Weak red | Angular blocky peds | × | 5.6 | 42.8 | 51.6 |
| WC-29 | Saprolite | 8.8 | B | 5R5/3 | Weak red | Angular blocky peds | × | 5.6 | 44.6 | 49.8 |
| WC-30 | Saprolite | 9.1 | B | 10R4/5 | Red | Angular blocky peds | × | 7.2 | 25.7 | 67.1 |
| WC-31 | Saprolite | 9.28 | B | 5R5/3 | Weak red | Angular blocky peds | × | 9.2 | 46.3 | 44.5 |
| WC-32 | Saprolite | 9.56 | B | 5R4/3 | Weak red | Angular blocky peds | × | 8.1 | 32.7 | 59.3 |
| WC-33 | Saprolite | 9.84 | B | 2.5YR5/3 | Reddish brown | Angular blocky peds | × | 7.6 | 39.1 | 53.3 |
| WC-34 | Saprolite | 10.12 | B | 2.5YR4/3 | Reddish brown | Angular blocky peds | × | 10.1 | 51.7 | 38.2 |
| WC-35 | Saprolite | 10.4 | B | 2.5YR4/4 | Reddish brown | Angular blocky peds | × | 9.5 | 53.8 | 36.7 |
| WC-36 | Saprolite | 10.68 | B | 10R4/6 | Red | Angular blocky peds | × | 10.2 | 41.6 | 48.2 |
| WC-37 | Saprolite | 10.96 | B | 10R4/5 | Red | Angular blocky peds | × | 7.7 | 46.5 | 45.9 |
| WC-38 | Saprolite | 11.24 | B | 5YR3/7 | Yellowish red | Angular blocky peds | × | 7.0 | 24.8 | 68.2 |
| WC-39 | Saprolite | 11.52 | B | 5YR3/6 | Yellowish red | Angular blocky peds | × | 6.8 | 45.1 | 48.1 |
| WC-40 | Saprolite | 11.8 | B | 10R4/5 | Red | Angular blocky peds | × | 7.9 | 30.2 | 61.8 |
| WC-41 | Saprolite | 12.08 | B | 10R4/6 | Red | Angular blocky peds | × | 11.8 | 46.5 | 41.6 |
| WC-42 | Saprolite | 12.36 | B | 10R4/5 | Red | Angular blocky peds | × | 7.5 | 33.1 | 59.4 |
| WC-43 | Saprolite | 12.64 | B | 5R4/3 | Weak red | Angular blocky peds | × | 8.9 | 43.7 | 47.4 |
| WC-44 | Saprolite | 12.92 | B | 2.5YR5/3 | Reddish brown | Angular blocky peds | × | 7.0 | 23.5 | 69.5 |
| WC-45 | Saprolite | 13.2 | B | 2.5YR4/3 | Reddish brown | Angular blocky peds | × | 7.0 | 23.9 | 69.1 |
| WC-46 | Saprolite | 13.48 | B | 2.5YR4/4 | Reddish brown | Angular blocky peds | × | 6.2 | 22.7 | 71.1 |
| WC-47 | Saprolite | 13.76 | B | 5YR3/7 | Yellowish red | Angular blocky peds | × | 6.3 | 26.3 | 67.4 |
| WC-48 | Saprolite | 14.04 | B | 5YR6/7 | Reddish yellow | Angular blocky peds | × | 6.7 | 30.6 | 62.7 |
| WC-49 | Saprolite | 14.32 | B | 5YR6/7 | Reddish yellow | Angular blocky peds | × | 5.6 | 22.4 | 72.0 |
| WC-50 | Saprolite | 14.6 | B | 5YR6/6 | Reddish yellow | Angular blocky peds | × | 5.4 | 28.9 | 65.7 |
| WC-51 | Saprolite | 14.88 | B | 5YR8/5 | Reddish yellow | Angular blocky peds | × | 6.3 | 30.5 | 63.2 |
| WC-52 | Saprolite | 15.16 | B | 5YR8/6 | Reddish yellow | Angular blocky peds | × | 6.3 | 29.1 | 64.6 |
| WC-53 | SWB[a] | 15.28 | C | 2.5YR7/3 | Light yellowish brown | Coarse platy peds | × | 3.8 | 27.2 | 69.0 |
| WC-54 | Basalt | 15.83 | R | 5G4/2 | Greylish green | | | | | |
| WC-55 | Basalt | 16.43 | R | 5G4/2 | Greylish green | | | | | |
| WC-56 | Basalt | 17.43 | R | 5G4/2 | Greylish green | | | | | |
| WC-57 | Basalt | 18.73 | R | 5G4/2 | Greylish green | | | | | |
| WC-58 | Basalt | 19.73 | R | 5G4/2 | Greylish green | | | | | |

[a] Semi-weathered basalt.

## B. Selection of reference element and element mobility

In order to evaluate the influence of reference element selection on mobility of elements, we calculated mass transfer ratios ($\tau$ values) for most elements by using Th, Nb, Zr, Ti as reference element, respectively. Except immobile elements (such as Al, Fe, Ti, Nb, Ta, Zr, Hf and Ga), for most elements and samples, reference element selection has very limited effect on $\tau$ value. For example, for sample WC-1 and Si, the $\tau_{Th,Si}$, $\tau_{Nb,Si}$, $\tau_{Zr,Si}$ and $\tau_{Ti,Si}$ values are $-0.79$, $-0.76$, $-0.74$ and $-0.73$, respectively, $-0.76 \pm 0.03$ (1s) on average. However, when Th was selected as reference element, there are distinct artificial depletions ($\tau_{Th,Nb}$ value is up to $-0.43$) for most immobile elements in certain Th and U rich sample (WC-30) (Fig. A1). When Nb, Zr and Ti were chosen as reference elements, this sample exhibits distinct enrichment of Th ($\tau_{Nb,Th}$ value is up to 0.76), corresponding to the abrupt increasing Th concentration of the sample. Moreover, for one special immobile element (such as Al) and sample WC-1, $\tau_{Th,Al}$, $\tau_{Nb,Al}$, $\tau_{Zr,Al}$ and $\tau_{Ti,Al}$ values are $-0.32$, $-0.24$, $-0.16$ and $-0.14$, respectively. These results indicate that when Zr and Ti were chosen as reference elements, the mobility of Al and Fe will be underestimated; Nb, Ta and Th can exhibit opposite enrichments or depletions in upper soil and saprolite samples, depending on the selection of reference element (Fig. A1).
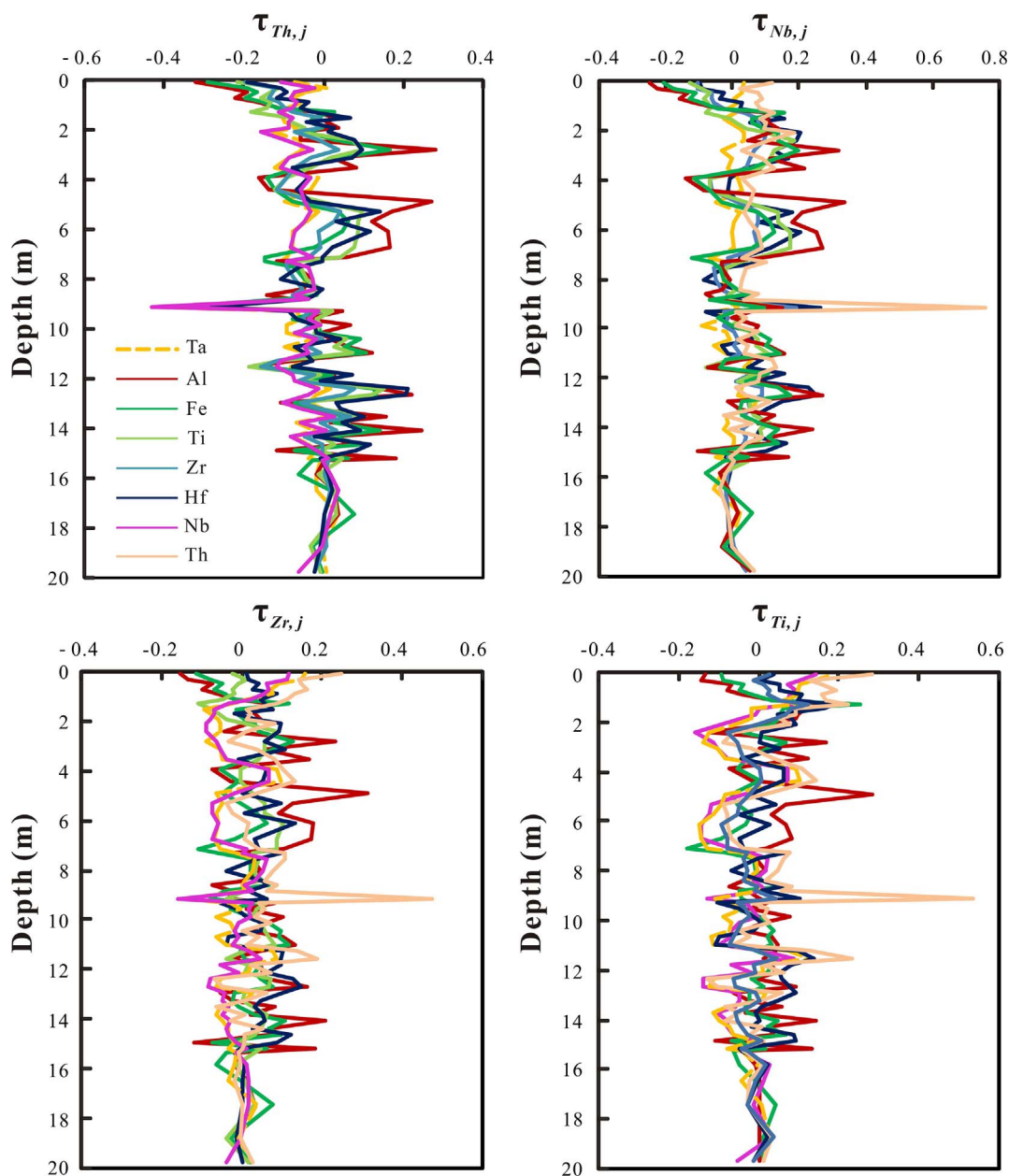
**Fig. A1.** The variation of mass transfer ratios (based on Th, Nb, Zr and Ti as reference element, respectively) for immobile elements along depth of the Wenchang weathering profile.

## References

Babechuk, M.G., Widdowson, M., Kamber, B.S., 2014. Quantifying chemical weathering intensity and trace element release from two contrasting basalt profiles, Deccan Traps, India. Chem. Geol. 363, 56–75.

Babechuk, M.G., Widdowson, M., Murphy, M., Kamber, B.S., 2015. A combined Y/Ho, high field strength element (HFSE) and Nd isotope perspective on basalt weathering, Deccan Traps, India. Chem. Geol. 396, 25–41.

Balan, E., Trocellier, P., Jupille, J., Fritsch, E., Muller, J.P., Calas, G., 2001. Surface chemistry of weathered zircons. Chem. Geol. 181, 13–22.

Behrends, T., Van Cappellen, P., 2005. Competition between enzymatic and abiotic reduction of uranium(VI) under iron reducing conditions. Chem. Geol. 220, 315–327.

Berger, A., Frei, R., 2014. The fate of chromium during tropical weathering: a laterite profile from Central Madagascar. Geoderma 213, 521–532.

Berner, R.A., Berner, E.K., 1997. Silicate weathering and climate. Tectonic Uplift and Climate Change. Springer, US, pp. 19–40.

Berner, R.A., Lasaga, A.C., Garrels, R.M., 1983. The carbonate–silicate geochemical cycle and its effect on atmospheric carbon-dioxide over the past 100 million years. Am. J. Sci. 283, 641–683.

Boekhout, F., Gerard, M., Kanzari, A., Michel, A., Dejeant, A., Galoisy, L., Calas, G., Descostes, M., 2015. Uranium migration and retention during weathering of a granitic waste rock pile. Appl. Geochem. 58, 123–135.

Bradl, H.B., 2004. Adsorption of heavy metal ions on soils and soils constituents. J. Coll. Interf. Sci. 277, 1–18.

Brantley, S.L., Lebedeva, M., 2011. Learning to read the chemistry of regolith to understand the Critical Zone. Annu. Rev. Earth Planet. Sci. 39, 387–416.

Braun, J.J., Ngoupayou, J.R.N., Viers, J., Dupré, B., Bedimo, J.P.B., Boeglin, J.L., Robain, H., Nyeck, B., Freydier, R., Nkamdjou, L.S., Rouiller, J., Muller, J.P., 2005. Present weathering rates in a humid tropical watershed: Nsimi, South Cameroon. Geochim. Comochim. Acta 69, 357–387.

Braun, J.J., Pagel, M., Herbilon, A., Rosin, C., 1993. Mobilization and redistribution of REEs and thorium in a syenitic lateritic profile: a mass balance study. Geochim. Comochim. Acta 57, 4419–4434.

Brookins, D.G., 1988. Eh-pH Diagrams for Geochemistry. Springer Verlag.

Chesworth, W., Duou, J., Larroque, P., 1981. The weathering of basalt and relative mobilities of the major elements at Belbex, France. Geochim. Comochim. Acta 45, 1235–1243.

Collins, R.N., Kinsela, A.S., 2010. The aqueous phase speciation and chemistry of cobalt in terrestrial environments. Chemosphere 79, 763–771.

Cornu, S., Lucas, Y., Lebon, E., Ambrosi, J.P., Luizão, F., Rouiller, J., Bonnay, M., Neal, C., 1999. Evidence of titanium mobility in soil profiles, Manus, central Amazonia. Geoderma 9, 281–295.

Dessert, C., Dupré, B., Gaillardet, J., François, L.M., Allègre, C.J., 2003. Basalt weathering laws and the impact of basalt weathering on the global carbon cycle. Chem. Geol. 202, 257–273.

Ding, C.P., 2008. Oxidation- reduction regimes and characteristics of natural soil, upland soil and paddy soil in China. Acta Pedol. Sin. 45, 66–75 (in Chinese with English abstract).

Dontsova, K., Zaharescu, D., Henderson, W., Verghese, S., Perdrial, N., Hunt, E., Chorover, J., 2014. Impact of organic carbon on weathering and chemical denudation of granular basalt. Geochim. Comochim. Acta 139, 508–526.

Driese, S.G., 2004. Pedogenic translocation of Fe in modern and ancient vertisols and implications for interpretations of the Hekpoort paleosol (2.25 Ga). J. Geol. 112, 543–560.

Driese, S.G., Peppe, D.J., Beverly, E.J., DiPietro, L.M., Arellano, L.N., Lehmann, T., 2016. Paleosols and paleoenvironments of the early Miocene deposits near Karungu, Lake Victoria, Kenya. Palaeogeogr. Palaeoclimatol. Palaeoecol. 443, 167–182.

Du, X., Rate, A.W., Gee, M.A.M., 2012. Redistribution and mobilization of titanium, zirconium and thorium in an intensely weathered lateritic profile in Western Australia. Chem. Geol. 330, 101–115.

Duff, M.C., Coughlin, J.U., Hunter, D.B., 2002. Uranium co-precipitation with iron oxide minerals. Geochim. Comochim. Acta 66, 3533–3547.

Dupré, B., Viers, J., Dandurand, J.L., Polve, M., Benezeth, P., Vervier, P., Braun, J.J., 1999. Major and trace elements associated with colloids in organic-rich river waters: ultrafiltration of natural and spiked solutions. Chem. Geol. 160, 63–80.

Ehrlich, H.L., 1998. Geomicrobiology: its significance for geology. Earth Sci. Rev. 45, 45–60.

Ellis, A.S., Johnson, T.M., Bullen, T.D., 2002. Chromium isotopes and the fate of hexavalent chromium in the environment. Science 295, 2060–2062.

Feng, J.L., 2010. Behaviour of rare earth elements and yttrium in ferromanganese concretions, gibbsite spots, and the surrounding terra rossa over dolomite during chemical weathering. Chem. Geol. 271, 112–132.

Fredrickson, J.K., Zachara, J.M., Kennedy, D.W., Duff, M.C., Gorby, Y.A., Li, S.M.W., Krupka, K.M., 2000. Reduction of U(VI) in goethite (α-FeOOH) suspensions by a dissimilatory metal-reducing bacterium. Geochim. Comochim. Acta 64, 3085–3098.

Gaillardet, J., Dupré, B., Louvat, P., et al., 1999. Global silicate weathering and $CO_2$ consumption rates deduced from the chemistry of large rivers. Chem. Geol. 159, 3–30.

Georg, R.B., Reynolds, B.C., West, A.J., Burton, K.W., Halliday, A.N., 2007. Silicon isotope variations accompanying basalt weathering in Iceland. Earth Planet. Sci. Lett. 261, 476–490.

Gislason, S.R., Arnorsson, S., 1993. Dissolution of primary basaltic minerals in naturalwaters-saturation state and kinetice. Chem. Geol. 105, 117–135.

Gislason, S.R., Oelkers, E.H., Eiriksdottir, E.S., Kardjilov, M.I., Gisladottir, G., Sigfusson, B., Snorrason, A., Elefsen, S., Hardardottir, J., Torssander, P., Oskarsson, N., 2009. Direct evidence of the feedback between climate and weathering. Earth Planet. Sci. Lett. 277, 213–222.

Guthrie, V.A., Kleeman, J.D., 1986. Changing uranium distributions during weathering of granite. Chem. Geol. 54, 113–126.

He, Y., Li, D.C., Velde, B., Yang, Y.F., Huang, C.M., Gong, Z.T., Zhang, G.L., 2008. Clay minerals in a soil chronosequence derived from basalt on Hainan Island, China and its implication for pedogenesis. Geoderma 148, 206–212.

Hill, I.G., Worden, R.H., Meighan, I.G., 2000. Yttrium: the immobility-mobility transition during basaltic weathering. Geology 28, 923–926.

Hodson, M.E., 2002. Experimental evidence for mobility of Zr and other trace elements in soils. Geochim. Comochim. Acta 66, 819–828.

Huang, C.M., Gong, Z.T., 2001. Geochemical implication of rare earth elements in process of soil development. J. Rare Earth 19, 57–62.

Huang, K.J., Teng, F.Z., Wei, G.J., Ma, J.L., Bao, Z.Y., 2012. Adsorption- and desorptioncontrolled magnesium isotope fractionation during extreme weathering of basalt in Hainan Island, China. Earth Planet. Sci. Lett. 359–360, 73–83.

Jahn, B.M., Gallet, S., Han, J.M., 2001. Geochemistry of the Xining, Xifeng and Jixian sections, Loess Plateau of China: aeolian dust provenance and paleosol evolution during the last 140 ka. Chem. Geol. 178, 71–94.

Jerden, J.L., Sinha, A.K., Zelazny, L., 2003. Natural immobilization of uranium by phosphate mineralization in an oxidizing saprolite-soil profile: chemical weathering of the Coles Hill uranium deposit, Virginia. Chem. Geol. 199, 129–157.

Jha, P.K., Tiwari, J., Singh, U.K., Kumar, M., Subramanian, V., 2009. Chemical weathering and associated $CO_2$ consumption in the Godavari river basin, India. Chem. Geol. 264, 364–374.

Ji, H.B., Wang, S.J., Ouyang, Z.Y., Zhang, S., Sun, C.X., Liu, X.M., Zhou, D.Q., 2004. Geochemistry of red residua underlying dolomites in karst terrains of YunnanGuizhou Plateau: I. The formation of the Pingba profile. Chem. Geol. 203, 1–27.

Jiang, J., Xu, R.K., Zhao, A.Z., 2011. Surface chemical properties and pedogenesis of tropical soils derived from basalts with different ages in Hainan, China. Catena 87, 334–340.

Jin, Z.D., Cao, J.J., Wu, J.L., Wang, S.M., 2006. A Rb/Sr record of catchment weathering response to Holocene climate change in Inner Mongolia. Earth Surf. Proc. Land. 31, 285–291.

Klinkhammer, G.P., Palmer, M.R., 1991. Uranium in the oceans: where it goes and why. Geochim. Comochim. Acta 55, 1799–1806.

Koppi, A.J., Edis, R., Field, D.J., Geering, H.R., Klessa, D.A., Cockayne, D.J.H., 1996. Rare earth element trends and cerium-uranium-manganese associations in weathered rock from Koongarra, northern territory, Australia. Geochim. Comochim. Acta 60, 1695–1707.

Kraemer, D., Kopf, S., Bau, M., 2015. Oxidative mobilization of cerium and uranium and enhanced release of "immobile" high field strength elements from igneous rocks in the presence of the biogenic siderophore desferrioxamine B. Geochim. Comochim. Acta 165, 263–279.

Kump, L.R., Brantley, S.L., Arthur, M.A., 2000. Chemical, weathering, atmospheric $CO_2$, and climate. Annu. Rev. Earth. Pl. Sci. 28, 611–667.

Kurtz, A.C., Derry, L.A., Chadwick, O.A., Alfano, M.J., 2000. Refractory element mobility in volcanic soils. Geology 28, 683–686.

Lerman, A., Wu, L.L., Mackenzie, F.T., 2007. $CO_2$ and $H_2SO_4$ consumption in weathering and material transport to the ocean, and their role in the global carbon balance. Mar. Chem. 106, 326–350.

Ling, S.X., Wu, X.Y., Ren, Y., Sun, C.W., Liao, X.N., Zhu, B.L., 2015. Geochemistry of trace and rare earth elements during weathering of black shale profiles in Northeast Chongqing, Southwestern China: their mobilization, redistribution, and fractionation. Chem. Erde-Geochem. 75, 403–417.

Liu, J.Q., Ren, Z.Y., Nichols, A.R.L., Song, M.S., Qian, S.P., Zhang, Y., Zhao, P.P., 2015. Petrogenesis of Late Cenozoic basalts from North Hainan Island: constraints from melt inclusions and their host olivines. Geochim. Comochim. Acta 152, 89–121.

Liu, S.A., Teng, F.Z., Li, S.G., Wei, G.J., Ma, J.L., Li, D.D., 2014. Copper and iron isotope fractionation during weathering and pedogenesis: insights from saprolite profiles. Geochim. Comochim. Acta 146, 59–75.

Liu, W.J., Liu, C.Q., Brantley, S.L., Xu, Z.F., Zhao, T., Liu, T.Z., Yu, C., Xue, D.S., Zhao, Z.Q., Cui, L.F., Zhang, Z.J., Fan, B.L., Gu, X., 2016. Deep weathering along a granite ridgeline in a subtropical climate. Chem. Geol. 427, 17–34.

Ma, J.L., Wei, G.J., Xu, Y.G., Long, W.G., 2010. Variations of Sr–Nd–Hf isotopic systematics in basalt during intensive weathering. Chem. Geol. 269, 376–385.

Ma, J.L., Wei, G.J., Xu, Y.G., Long, W.G., Sun, W.D., 2007. Mobilization and re-distribution of major and trace elements during extreme weathering of basalt in Hainan Island, South China. Geochim. Comochim. Acta 71, 3223–3237.

Marques, J.J., Schulze, D.G., Curi, N., Mertzman, S.A., 2004. Trace element geochemistry in Brazilian Cerrado soils. Geoderma 121, 31–43.

Middelburg, J.J., Van der Weijden, C.H., Woittiez, J.R.W., 1988. Chemical processes affecting the mobility of major, minor, and trace elements during weathering of granitic rocks. Chem. Geol. 68, 253–273.

Mucci, A., Morse, J.W., 1983. The incorporation of $Mg^{2+}$ and $Sr^{2+}$ into calcite overgrowths: influences of growth rate and solution composition. Geochim. Comochim. Acta 47, 217–233.

Navarre-Sitchler, A., Brantley, S., 2007. Basalt weathering across scales. Earth Planet. Sci. Lett. 261, 321–334.

Nesbitt, H.W., 1979. Mobility and fractionation of Rare-Earth elements during weathering of a granodiorite. Nature 279, 206–210.

Nesbitt, H.W., Markovics, G., 1997. Weathering of granodioritic crust, long-term storage of elements in weathering profiles, and petrogenesis of siliciclastic sediments. Geochim. Comochim. Acta 61, 1653–1670.

Nesbitt, H.W., Markovics, G., Price, R.C., 1980. Chemical processes affecting alkalis and alkaline earths during continental weathering. Geochim. Comochim. Acta 44, 1659–1666.

Nesbitt, H.W., Wilson, R.E., 1992. Recent chemical weathering of basalts. Am. J. Sci. 292, 740–777.

Nesbitt, H.W., Young, G.M., 1982. Early proterozoic climates and plate motions inferred from major element chemistry of lutites. Nature 299, 715–717.

Nesbitt, H.W., Young, G.M., 1989. Formation and diagenesis of weathering profiles. J. Geol. 97, 129–147.

O'Connor, A.E., Luek, J.L., McIntosh, H., Beck, A.J., 2015. Geochemistry of redox-sensitive trace elements in a shallow subterranean estuary. Mar. Geol. 172, 70–81.

Oliva, P., Viers, J., Dupré, B., Fortuné, J.P., Martin, F., Braun, J.J., Robain, H., 1999. The effect of organic matter on chemical weathering: study of a small tropical watershed: Nsimi-Zoétélé site. CameroonGeochim. Comochim. Acta 63, 4013–4035.

Oze, C., Bird, D.K., Fendorf, S., 2007. Genesis of hexavalent chromium from natural sources in soil and groundwater. P. Natl. Acad. Sci. USA 104, 6544–6549.

Pokrovsky, O.S., Schott, J., 2002. Iron colloids/organic matter associated transport of major and trace elements in small boreal rivers and their estuaries (NW Russia). Chem. Geol. 190, 141–179.

Pokrovsky, O.S., Schott, J., Dupré, B., 2006. Basalt weathering and trace elements migration in the boreal Arctic zone. J. Geochem. Explor. 88, 304–307.

Poszwa, A., Dambrine, E., Pollier, B., Atteia, O., 2000. A comparison between Ca and Sr cycling in forest ecosystems. Plant Soil. 225, 299–310.

Prunier, J., Chabaux, F., Stille, P., Gangloff, S., Pierret, M.C., Viville, D., Aubert, A., 2015. Geochemical and isotopic (Sr, U) monitoring of soil solutions from the Strengbach catchment (Vosges mountains, France): evidence for recent weathering evolution. Chem. Geol. 417, 289–305.

Ratié, G., Jouvin, D., Garnier, J., Rouxel, O., Miska, S., Guimarães, E., Vieira, L.C., Sivry, Y., Zelanod, I., Montargès-Pelletier, E., Thil, F., Quantin, C., 2015. Nickel isotope fractionation during tropical weathering of ultramafic rocks. Chem. Geol. 402, 68–76.

Rye, R., Holland, H.D., 2000. Geology and geochemistry of paleosols developed on the Hekpoort basalt, Pretoria Group, South Africa. Am. J. Sci. 300, 85–141.

Sak, P.B., Fisher, D.M., Gardner, T.W., Murphy, K., Brantley, S.L., 2004. Rates of weathering rind formation on Costa Rican basalt. Geochim. Comochim. Acta 68, 1453–1472.

Sak, P.B., Navarre-Sitchler, A.K., Miller, C.E., Daniel, C.C., Gaillardet, J., Buss, H.L., Lebedeva, M.I., Brantley, S.L., 2010. Controls on rind thickness on basaltic andesite clasts weathering in Guadeloupe. Chem. Geol. 276, 129–143.

Scott, C., Lyons, T.W., Bekker, A., Shen, Y., Poulton, S.W., Chu, X., Anbar, A.D., 2008. Tracing the stepwise oxygenation of the Proterozoic ocean. Nature 452, 456–459.

Tejian-kella, M.S., Fitzpatrick, R.W., Chittleborough, D.J., 1991. Scanning electron microscope study of zircons and rutiles from a podzol chronosequence at Cooloola, Queensland, Australia. Catena 18, 11–30.

Teng, F.Z., Li, W.Y., Rudnick, R.L., Gardner, L.R., 2010. Contrasting lithium and magnesium isotope fractionation during continental weathering. Earth Planet. Sci. Lett. 300, 63–71.

Topp, S.E., Salbu, B., Roaldset, E., Jorgensen, P., 1984. Vertical distribution of trace

elements in a laterite soil (Suriname). Chem. Geol. 47, 159–174.

Torrent, J., Schwertmann, U., Fechter, H., Alferez, F., 1983. Quantitative relationships between soil color and hematite content. Soil Sci. I36, 354–358.

Van der Weijden, C.H., Van der Weijden, R.D., 1995. Mobility of major, minor and some redox sensitive trace elements and rare-earth elements during weathering of four granitoids in central Portugal. Chem. Geol. 125, 149–167.

Viers, J., Dupré, B., Braun, J.J., Deberdt, S., Angeletti, B., Ngoupayou, J.N., Michard, A., 2000. Major and trace element abundances, and strontium isotopes in the Nyong basin rivers (Cameroon): constraints on chemical weathering processes and elements transport mechanisms in humid tropical environments. Chem. Geol. 169, 211–241.

Vircava, I., Somelar, P., Liivamägi, S., Kirs, J., Kirsimäe, K., 2015. Origin and paleoenvironmental interpretation of aluminum phosphate–sulfate minerals in a Neoproterozoic Baltic paleosol. Sediment. Geol. 319, 114–123.

Walter, A.V., Nahon, D., Flicoteaux, R., Girard, J.P., Melfi, A., 1995. Behaviour of major and trace elements and fractionation of REE under tropical weathering of a typical apatite-rich carbonatite from Brazil. Earth Planet. Sci. Lett. 136, 591–602.

Wang, L., Zhang, L.J., Cai, W.J., Wang, B.S., Yu, Z.G., 2016. Consumption of atmospheric CO2 via chemical weathering in the Yellow River basin: the Qinghai-Tibet Plateau is the main contributor to the high dissolved inorganic carbon in the Yellow River. Chem. Geol. 430, 34–44.

Wang, Q.L., Chetelat, B., Zhao, Z.Q., Ding, H., Li, S.L., Wang, B.L., Li, J., Liu, X.L., 2015. Behavior of lithium isotopes in the Changjiang River system: sources effects and response to weathering and erosion. Geochim. Comochim. Acta 151, 117–132.

Young, G.M., Nesbitt, H.W., 1998. Processes controlling the distribution of Ti and Al in weathering profiles, siliciclastic sediments and sedimentary rocks. J. Sediment. Res. 68, 448–455.

Zhang, Z.J., Liu, C.Q., Zhao, Z.Q., Cui, L.F., Liu, W.J., Liu, T.Z., Liu, B.J., Fan, B.L., 2015. Behavior of redox-sensitive elements during weathering of granite in subtropical area using X-ray absorption fine structure spectroscopy. J. Asian. Earth. Sci. 105, 418–429.